Understanding the ENSO–CO_2 Link Using Stabilized Climate Simulations

SAMANTHA STEVENSON AND BAYLOR FOX-KEMPER

Department of Atmospheric and Oceanic Sciences, University of Colorado, Boulder, Colorado

MARKUS JOCHUM

National Center for Atmospheric Research, Boulder, Colorado*

(Manuscript received 24 September 2011, in final form 20 May 2012)

ABSTRACT

The influence of atmospheric CO_2 concentration on the El Niño–Southern Oscillation (ENSO) is explored using 800-yr integrations of the NCAR Community Climate System Model, version 3.5 (CCSM3.5), with CO_2 stabilized at the A.D. 1850, 1990, and 2050 levels. Model mean state changes with increased CO_2 include preferential SST warming in the eastern equatorial Pacific, a weakening of the equatorial trade winds, increased vertical ocean stratification, and a reduction in the atmospheric Hadley and oceanic subtropical overturning circulations. The annual cycle of SST strengthens with CO_2, likely related to unstable air–sea interactions triggered by an increased Northern Hemisphere land–sea temperature contrast. The mean trade wind structure changes asymmetrically about the equator, with increased convergence in the Northern Hemisphere and divergence in the Southern Hemisphere leading to corresponding deepening and shoaling of the thermocline. The proportion of eastern versus central Pacific–type El Niño events increases with CO_2, but the significance of the changes is relatively low; ENSO amplitude also increases with CO_2, although the change is insignificant at periods longer than 4 yr. The 2–4-yr ENSO response shows an enhancement in equatorial Kelvin wave variability, suggesting that stochastic triggering of El Niño events may be favored with higher CO_2. However, the seasonal cycle–ENSO interaction is also modified by the asymmetric climatological changes, and forcing by the Southern Hemisphere becomes more important with higher CO_2. Finally, higher-resolution CCSM4 control simulations show that ENSO weakens with CO_2 given a sufficiently long integration time. The cause for the difference in ENSO climate sensitivity is not immediately obvious but may potentially be related to changes in westerly wind bursts or other sources of high-frequency wind stress variability.

1. Introduction

Understanding how the El Niño–Southern Oscillation (ENSO) may change in the future is a critical environmental issue (Ropelewski and Halpert 1996; Rajagopalan and Lall 1998; Whetton et al. 1990) that remains poorly understood. Typically ENSO projections are conducted using general circulation models (GCMs), but multimodel studies of the ENSO climate change response show large disagreements in both the direction and magnitude of twenty-first-century changes (AchutaRao and Sperber 2006; Guilyardi 2006; Collins et al. 2010). There remain several obstacles to constraining future ENSO changes using climate models, which may be summarized as the following: insufficient observations to obtain robust ENSO statistics, the potential presence of slow ENSO adjustments to changing CO_2, and biases in representations of ENSO-relevant physical processes. To date, no modeling experiment has been constructed that can isolate the influence of CO_2 changes in the absence of these effects; this study is designed to close that gap.

Determining the required record length to constrain ENSO statistics is not a trivial calculation, as basinwide real-time monitoring of Pacific Ocean conditions only began in the 1980s, with the creation of the Tropical Atmosphere Ocean (TAO) buoy array (McPhaden et al. 1998). Observations were more sparse prior to this, though SST has been reconstructed as far back as the

* The National Center for Atmospheric Research is sponsored by the National Science Foundation.

Corresponding author address: Samantha Stevenson, International Pacific Research Center, University of Hawaii at Manoa, POST 401, Honolulu, HI 96822.
E-mail: slgs@hawaii.edu

DOI: 10.1175/JCLI-D-11-00546.1

nineteenth century (i.e., Smith and Reynolds 2004; Rayner et al. 2006). Given the limitations of the observational record, the causes and extent of natural ENSO variations are difficult to pin down precisely (Ropelewski and Halpert 1986; Trenberth and Hurrell 1994). ''Regime shifts'' have occurred even during the twentieth century (Miller et al. 1994), indicating that natural variability may potentially be quite large.

Longer ENSO time series created with GCMs show substantial natural variability as well. Simulations carried out by Wittenberg (2009) using the Geophysical Fluid Dynamics Laboratory Climate Model version 2.1 (GFDL CM2.1) have shown that unforced centennial variations in ENSO amplitude of a factor of 2 or more may occur, and that several centuries of model output are required for the system to ''converge'' to stable statistics. Stevenson et al. (2010) quantified the convergence relationship using a wavelet-based technique, and found that roughly 240 yr of observations would be needed to constrain the real ENSO, assuming that the background climate was stable. Thus, a great deal of the uncertainties associated with twenty-first-century projections could potentially be due to sampling bias.

Bias from using short simulations can be mitigated by running multiple ensemble members; averaging many realizations of the climate provides a more robust estimate. But this may not be completely satisfactory, as shown by Stevenson et al. (2012) using the five- to six-member twentieth- and twenty-first-century Community Climate System Model, version 4 (CCSM4) ensembles. Despite containing a total of more than 500 model years, the ensembles showed no significant ENSO amplitude response to CO_2. This may be due to the fact that the ocean is continually adjusting to rapidly changing CO_2 forcing over the course of the twenty-first century. The precise extent of transient mean state influences on ENSO remains unclear, but a preliminary analysis of Coupled Model Intercomparison Project phase 5 (CMIP5) simulations indicates that the magnitudes of twenty-first-century and mean-state changes are not strongly related (Stevenson 2012). The ENSO response to slow ocean adjustment remains to be thoroughly investigated.

If the projections used to analyze future ENSO changes are too short individually, and slow ocean adjustment introduces biases that cannot be eliminated by large ensembles, then the overall ENSO climate sensitivity remains an unknown. In this case, very long equilibrated simulations at varying CO_2 concentrations are necessary to determine whether the ENSO sensitivity indeed differs between models. Here the focus is purely on the physics of the equilibrated changes to ENSO due to CO_2 increases, in the absence of transient effects. It is hoped that these results will serve to motivate similar experiments with other models.

The structure of the paper is as follows: The model experiments are described in section 2. Changes to the mean atmosphere–ocean circulation are presented in section 3. The responses of ENSO and El Niño event types to CO_2 increases are discussed in section 4, the annual cycle response in section 5, and the response of 2–4-yr variability changes in section 6. Variability at longer periods is discussed briefly in section 7, and implications of intermodel differences for CMIP discussed in section 8. Finally, conclusions are provided in section 9.

2. Experimental setup

The numerical experiments are performed using the National Center for Atmospheric Research (NCAR) Community Climate System Model, version 3.5 (CCSM3.5) in the fully coupled configuration (active atmosphere, ocean, land, and sea ice). The ocean model has a zonal resolution that varies from 340 km at the equator to 40 km around Greenland, and a meridional resolution that varies from 70 km at the equator to 40 km around Greenland and 350 km in the North Pacific. This spatially varying resolution is achieved by placing the north pole of the grid over Greenland and reflects the different relevant length scales of two processes that are important in maintaining a stable global climate: deep convection around Greenland and in the Arctic and oceanic heat uptake at the equator. In the vertical there are 25 depth levels; the uppermost layer has a thickness of 8 m and the deepest layer has a thickness of 500 m. The atmospheric model uses T31 spectral truncation in the horizontal (about 3.75° resolution) with 26 vertical levels. The sea ice model shares the same horizontal grid as the ocean model, and the land model is on the same horizontal grid as the atmosphere. This setup (called T31 $\times$ 3) has been developed specifically for long paleoclimate and biogeochemistry integrations, and its performance is described in detail by Yeager et al. (2006). The most significant difference between the present model setup (CCSM3.5) and the one described in Yeager et al. (2006) is the new atmospheric convection scheme, which leads to significant improvements in the simulation of ENSO in the high-resolution (Neale et al. 2008) and present coarse-resolution configurations (Jochum et al. 2010). Changes to the ocean GCM are a stratification-dependent thickness diffusivity (Danabasoglu and Marshall 2007) that improves the equatorial thermocline, a reduced viscosity (Jochum et al. 2008) that improves the equatorial

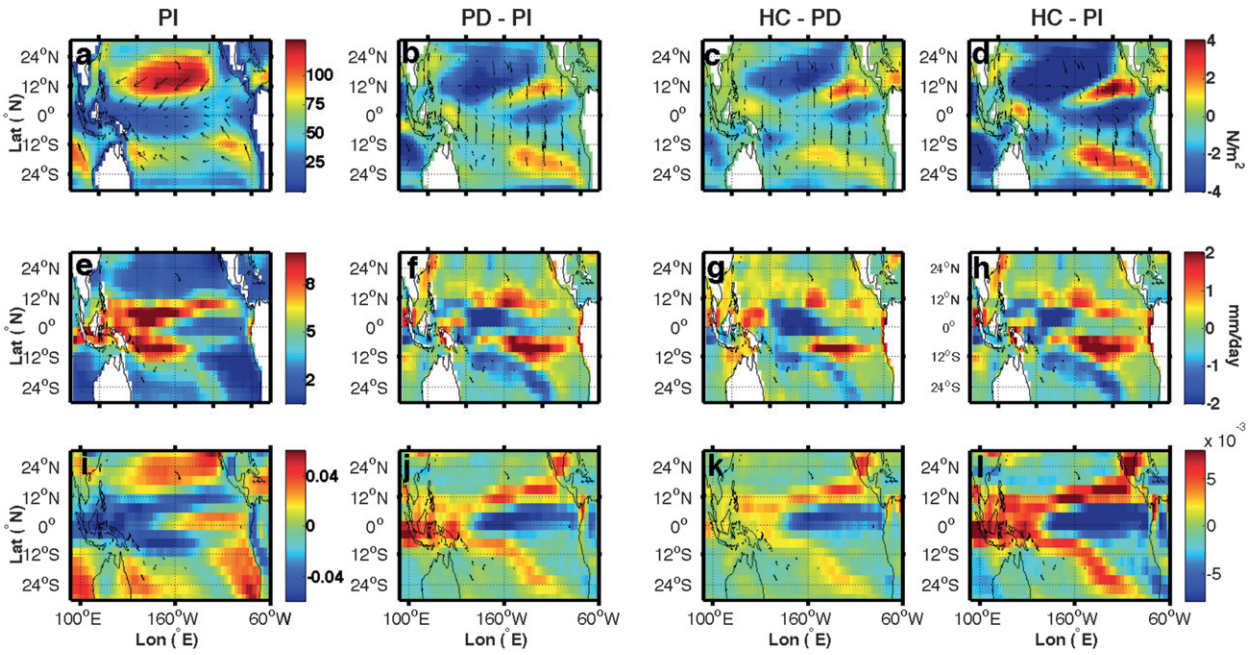

FIG. 1. Changes to the mean state of the atmosphere: (a),(e),(i) mean state for PI; and differences between (b),(f),(j) PD and PI; (c),(g),(k) HC and PD; and (d),(h),(l) HC and PI. (a)–(d) Differences in wind stress (arrows show direction, colors show the magnitude of the wind stress difference). (e)–(h),(i)–(l) As in (a)–(d), but for precipitation, and ω_{500}, respectively.

surface currents, and an increased background diapycnal diffusivity (Jochum 2009) that stabilizes the meridional overturning circulation.

Three integrations of the T31 × 3 CCSM3.5 have been carried out, each of which covers 1000 model years. The three model simulations were initialized from the climatology of Levitus (1998) and subsequently run without external forcing: each reached equilibrium after roughly 200 model years.[1] The equilibrium solution is therefore considered to consist of model years 200–1000 for each simulation. The only parameter that changes between the simulations is the atmospheric CO_2 concentration; values of 255, 355, and 455 ppm are adopted to sample the range of concentrations expected over the time period 1850–2050. Hereafter, the simulations are referred to as ''preindustrial'' (PI; 255 ppm), ''present day'' (PD; 355 ppm), and ''high CO_2'' (HC; 455 ppm).

3. Mean circulation changes

ENSO dynamics are often described through linkages with the atmosphere–ocean mean state (Fedorov and Philander 2000, 2001; Timmermann et al. 1999), although there is still some debate over the role of long-term modulations in the mean state on ENSO and vice versa (Sun 2003; Sun and Zhang 2006). Here, both the mean state and the general circulation of the atmosphere and ocean are examined.

In the atmosphere, the most relevant variables are the wind stress τ, precipitation P, and vertical pressure velocity at 500 hPa ω_{500}: changes between simulations are shown in Fig. 1. The overall trade winds weaken with CO_2, consistent with results from Vecchi and Soden (2007) and Held and Soden (2006), which suggested that the strength of the Hadley and Walker cells should decrease in a warmer climate because of the decrease in convective exchange between the boundary layer and free troposphere required by the slower increase in precipitation relative to humidity.

The magnitude of changes to the Walker circulation is not quantified here, but these results are consistent with both an eastward shift and a weakening. The eastward shift is indicated by the changes to the mean ω_{500} and precipitation in Fig. 1; enhanced precipitation is seen in the eastern Pacific (EP) and a reduction in the west. Corresponding changes are seen in ω_{500}. Changes in the overall strength of the circulation may be roughly estimated by examining changes to the maximum value of ω_{500}, which are on the order of 10%–15% in the eastern Pacific (Figs. 1e–g). Anomalies in ω_{500} generally oppose the structure of mean ω_{500} in the tropics; thus, the Walker circulation can be presumed to weaken, even as

[1] Some residual spinup effects remain in the deep (≥1000 m) ocean but are not expected to greatly impact ENSO dynamics.

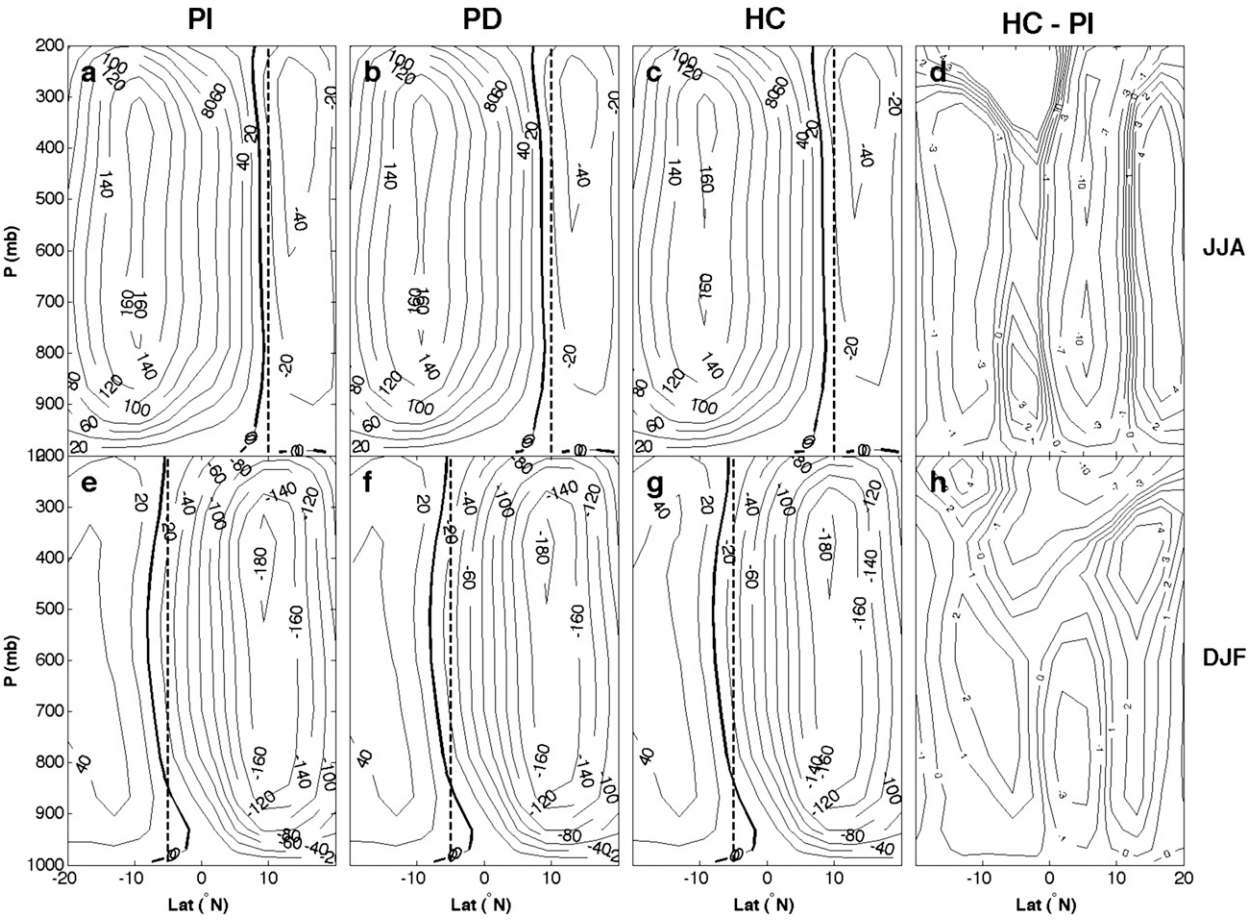

FIG. 2. Changes to the atmospheric overturning streamfunction (Sv; 1 Sv = 10^9 kg s^{-1}) corresponding to the strength of the Hadley cell. Here positive values correspond to a counterclockwise circulation, negative values to clockwise circulation. The zero contour is thick. Vertical dashed lines indicate the locations of 10°N and 5°S and are provided for visual context. (a)–(c) JJA mean for PI, PD, and HC, respectively and (d) difference between JJA means for HC and PI. (e)–(h) As in (a)–(d), but for DJF.

the convective center shifts eastward. Additionally, the overall subtropical meridional wind stress changes are consistent with a weakening of the Hadley cell (Figs. 1b,c): southerly (northerly) anomalies dominate in the Northern (Southern) Hemisphere. The weakening of the Walker circulation then follows from continuity.

To further quantify the reduction in the Hadley circulation, the atmospheric overturning streamfunction is calculated and plotted in Fig. 2. The formulation of the streamfunction follows Döös and Nilsson (2011): in pressure coordinates,

$$\Phi(y,P)=\frac{1}{t-t_0}\int_{t_0}^{t}\oint\int_0^P\frac{v(x,y,P',t)}{g}\,dP'\,dx\,dt. \quad (1)$$

The circulation is plotted separately for December–February (DJF) and June–August (JJA) to allow for ease of interpretation. During JJA, the northern Hadley cell weakens slightly (~10% of the PI value) and shifts slightly to the south, as indicated by the position of the zero contour in Fig. 2c. Negative anomalies in Fig. 2d also show the weakening of the Southern Hemisphere branch of the circulation. The changes during DJF are smaller, only 1%–2% of the PI streamfunction, and show less spatial coherence than the JJA anomalies. A small tendency toward poleward contraction may be evident in both branches (Figs. 2d,h), but the dominant influence is the boreal summer shift (Figs. 2a–d).

A weakening of the Hadley circulation, even during the summer months alone, has several implications. First, the associated reduction in the zonal trade winds will tend to be larger at higher latitudes, since the Coriolis force on the surface flow is stronger farther from the equator. This in turn leads to a reduction in the subtropical wind stress curl, which can be seen in Figs. 1b,c. A weaker wind stress curl will then slow subduction

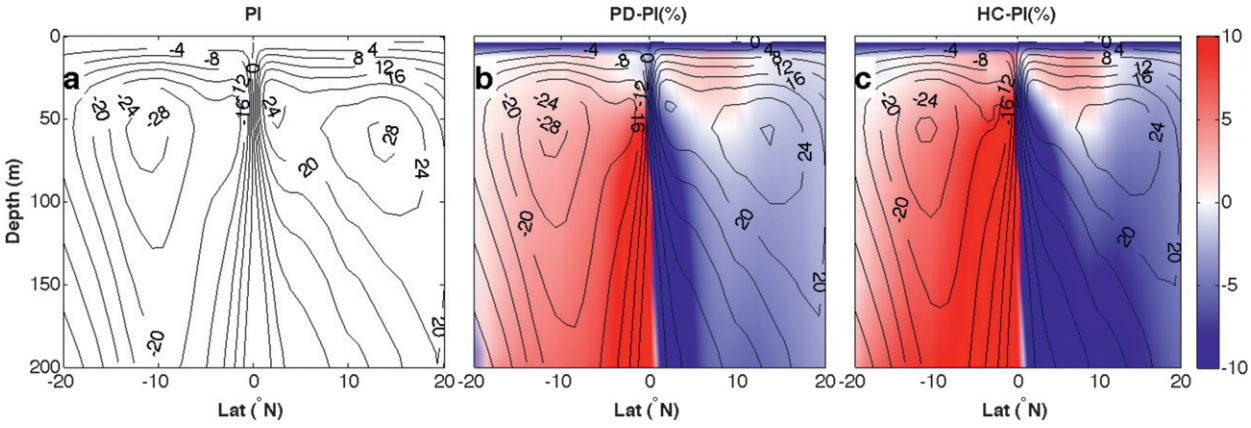

FIG. 3. Summary of the circulation of the tropical Pacific. Overturning streamfunction for the STC (Sv). The contours indicate streamfunction magnitude, while the colors show the percentage change relative to PI.

and affect circulation in the subtropical cell (STC), and therefore be felt by the equatorial ocean.

To directly assess changes to the subtropical cell in relation to Ekman pumping, a summary of both quantities is provided in Fig. 3. The formulation of the oceanic meridional overturning streamfunction used in Fig. 3 is

$$\Phi = \int_{z_0}^{z} v(y,z)\,dz - \int_{y_0}^{y} w(y,z_0)\,dy, \qquad (2)$$

since now depth coordinates are used. Figure 3 indicates the reduction in equatorial upwelling, which shrinks by 5%–10% in HC relative to PI (Fig. 3f). Circulation along the poleward edges of the STC also decreases with CO_2 by 10%–20% (Figs. 3b,c), which may be interpreted as a contraction of the overturning circulation due to the reduction in off-equatorial wind stress curl near 10°N/S (cf. Figs. 1a–d). It should also be noted that there is a small (5%–10%) increase in circulation in the core of the STC in HC and PD relative to PI, near 5°–10°N. This increase is likely related to the climatological changes in the wind stress, which tend to favor enhanced convergence in the Northern Hemisphere (Fig. 1).

The change to the oceanic mean state is shown in Fig. 4 and reveals several crucial features: the enhanced SST warming in the eastern Pacific (i.e., the weakened cold tongue; Figs. 4b,c) and the increase in equatorial stratification (Figs. 4j,k). Changes to the off-equatorial thermocline (defined using the 20°, 20.5°, and 21°C isotherms in PI, PD, and HC, respectively) are asymmetric about the equator in Figs. 4f–h. There is a pronounced deepening near 10°N, with a corresponding shoaling near 10°S. This is likely due to the asymmetric changes in the mean wind stress, which were shown by Xie et al. (2010) to relate to wind–evaporation–SST (WES) feedback. The hemispherically asymmetric response of the mean thermocline has implications for its response to seasonally forced changes, which will be shown in later sections to be of crucial importance for ENSO.

The stratification increase is related to the change in the Hadley circulation through its connection with the subtropical cell. A decrease in heat flux divergence from the equatorial region as the climate warms is a known feature of coupled GCMs (Collins et al. 2010; Vecchi and Soden 2007) and should be expected to lead to an enhanced warming along the equator relative to higher latitudes. Likewise, Liu and Philander (1995) showed that a weaker subtropical wind stress curl leads to less warm water being transported to the lower equatorial thermocline, increasing equatorial stratification. Thus, Fig. 3 serves as a confirmation of well-understood dynamical changes.

The increase in vertical stratification and reduction in subtropical wind stress curl seen in Figs. 1 and 4 are expected to be accompanied by a shoaling of the mean thermocline. Is the expected degree of shoaling sufficient to explain the changes in Figs. 4e,f? The scaling relationship developed by Luyten et al. (1983) and reproduced in Pedlosky (1996; hereafter, the LPS scaling) is applied to these simulations to assess whether any further exploration of the thermocline shift is necessary. The LPS scaling relationship is given by

$$H = \sqrt{\frac{\tau_0 L}{\gamma_2 \rho_0}}, \qquad (3)$$

where τ_0 is the mean subtropical wind stress, L the size of the basin, ρ_0 the mean density of seawater, and γ_2 the scaled difference in density for water above and below

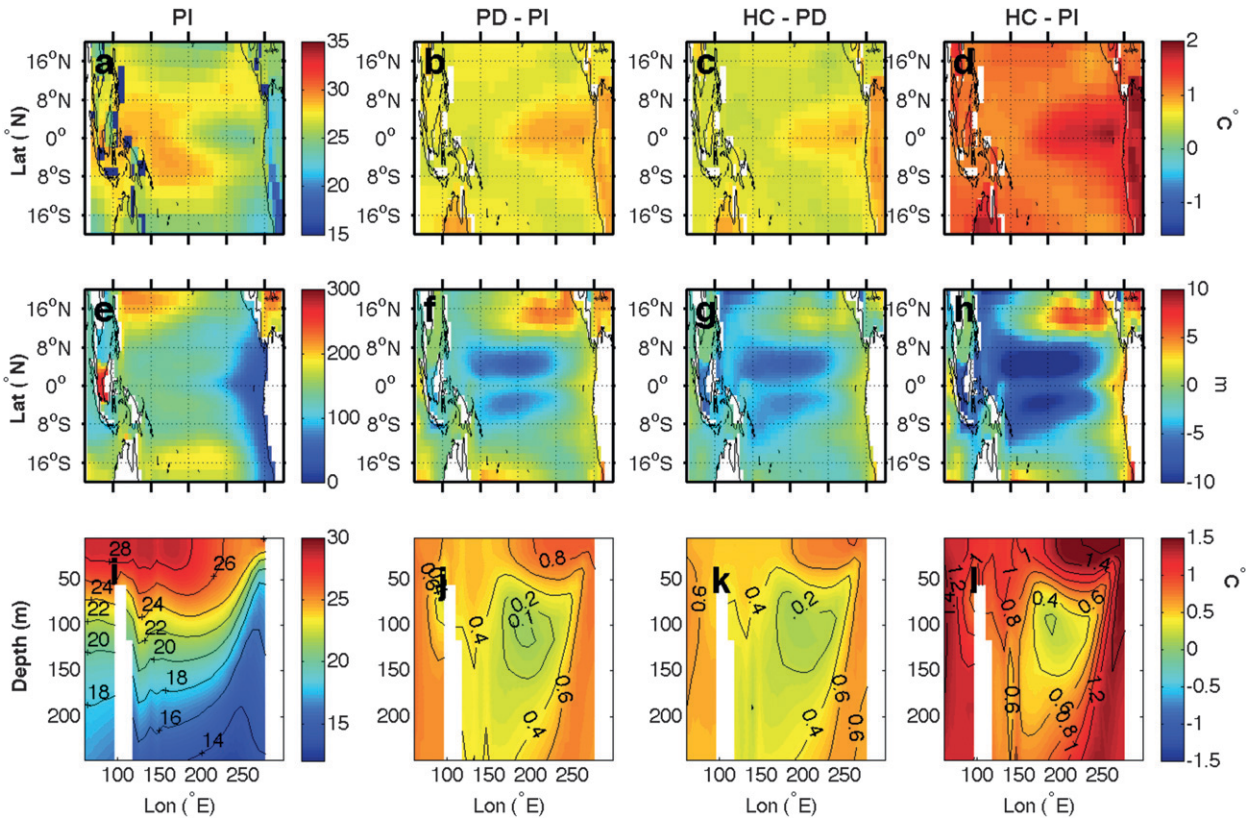

FIG. 4. Changes to the mean state of the ocean. (a),(e),(i) The mean for the PI simulation; and differences between (b),(f),(j) PD and PI; (c),(g),(k) HC and PD; and (d),(h),(l) HC and PI for (a)–(d) SST (°C), (e)–(h) thermocline depth (m), and (i)–(l) subsurface temperature (°C), averaged over 5°N–5°S.

the thermocline, given by $\gamma_2 = [(\rho_2 - \rho_1)/\rho_0] \times g$. Here, τ_0 and γ_0 have been calculated from the CCSM3.5 output and are provided in Table 1, along with the other constants used in Eq. (3). When the mean thermocline is calculated using this relationship, the result ranges from 120 to 106 m, values that are remarkably consistent with the climatological mean thermocline depth in the ocean model. The equatorial thermocline is somewhat shallower (Table 1) but changes in depth with CO_2 are similar to those in the extratropics.

Thermocline changes from Eq. (3) are next compared with the thermocline depths in CCSM3.5. Here the thermocline in the Niño-3.4 region has been calculated based on the position of the maximum vertical temperature gradient, and the result averaged in time and space. Values are generally shallower than the H values from Eq. (3), ranging from 92 to 74 m. The percentage change from PI to PD is somewhat larger than the 6% predicted by the LPS scaling, but the PD–HC shoaling is nearly identical. The thermocline is therefore presumed to be set primarily by nondissipative processes, and thermocline changes presumed to be a straightforward consequence of shifts in the general circulation.

TABLE 1. Estimates of thermocline depth for the CCSM3.5 simulations. Here, H indicates the thermocline depth calculated from the scaling relationships of Pedlosky (1996), using the state variables obtained from each simulation, and Z_{mn} is the thermocline depth calculated directly from CCSM3.5, using the depth at which the vertical temperature gradient is at a maximum. Zonal wind stress is averaged over the so-called matching region in the subtropics, here defined as 10°–20°N, 190°–240°E. The difference γ_2 is calculated using potential densities above and below the main pycnocline in the Niño-3.4 region: averaging depths are 0–50 m for the upper layer and 100–150 m for the lower layer. The depth Z_{mn} is calculated over the Niño-3.4 region.

Simulation	L (km)	τ_x (N m^{-2})	γ_2 (kg m^{-3})	ρ_0 (kg m^{-3})	H (m)	Z_{mn} (m)
PI	3000	−0.0963	−0.0193	1025	120.8	92.3
PD	3000	−0.0947	−0.0218	1025	112.8	79.3
HC	3000	−0.0929	−0.0240	1025	106.5	74.5

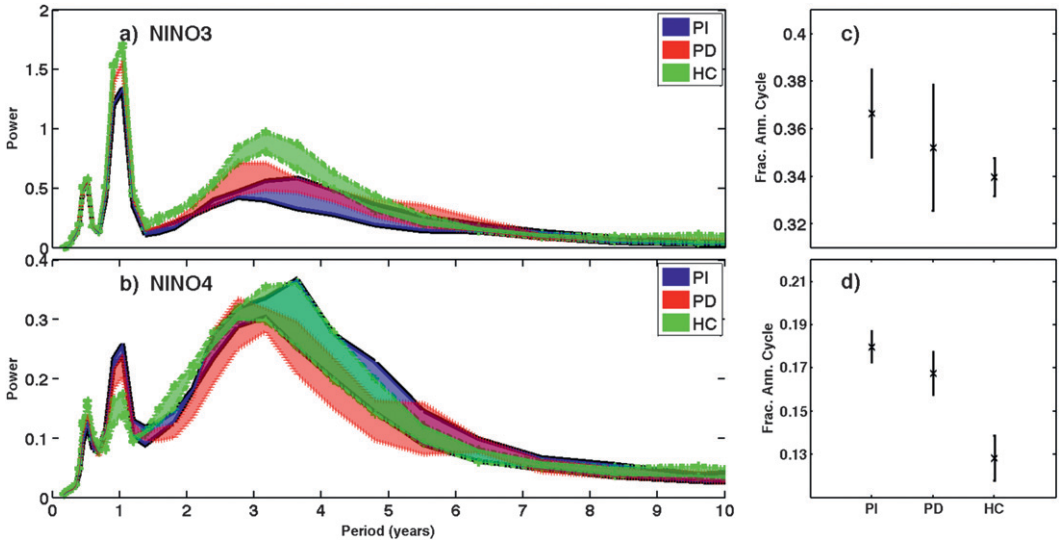

FIG. 5. (a),(b) Spectral range for 100-yr subintervals taken from each of the three equilibrated CCSM3.5 simulations: PI (255 ppm CO_2), PD (355 ppm CO_2), and HC (455 ppm CO_2). (a),(c) Niño-3 SST and (b),(d) Niño-4 SST. All wavelet power values are given in °C^2. The fraction of total Niño-3 and Niño-4 wavelet power found in the annual cycle (defined as periods between 0.75 and 1.25 yr) is provided in (c),(d).

4. ENSO response

Measuring changes to ENSO amplitude requires choosing an appropriate metric; here the Niño-3 (5°S–5°N, 90°–150°W), Niño-4 (5°S–5°N, 160°E–150°W), and Niño-3.4 (5°S–5°N, 120°–170°W) SST time series are adopted. The spectral range of Niño-3 and Niño-4 SST, generated from successive 100-yr subintervals of each simulation, is shown in Fig. 5. Spectra are calculated using the wavelet toolkit of Torrence and Compo (1998), with the bias correction of Liu et al. (2007) applied to prevent artificial enhancement at long periods. The "envelopes" in Fig. 5 do overlap, but there is a distinct trend toward high amplitude with CO_2 in the eastern Pacific, which is especially apparent in Niño-3 SST. No notable changes in the overall ENSO period are visible in Fig. 5, given the broad spectral peak.

The bandpassed[2] variance constitutes a good first-order diagnostic for the significance of ENSO changes. Previous results (Wittenberg 2009; Stevenson et al. 2010) showed that several hundred years of data are required for convergence to a stable "background" ENSO state, and this is upheld in the variance plots in Fig. 6. The 90% confidence intervals are constructed by selecting random subsamples of a specified length—when 30 yr is used, the 2–4-yr confidence intervals overlap for all simulations. Confidence interval width decreases with sampling length, and the PI/HC offset becomes significant at record lengths of about 300–400 yr. Strikingly, even at 400 yr, PD and HC remain indistinguishable, an indication of the importance of the degree of CO_2 increase for ENSO changes on long time scales.

The behavior of the 5–7-yr bandpass-filtered variance differs greatly from that of 2–4 yr. Rather than a monotonic increase with CO_2, there is an enhancement in PD relative to both PI and HC. Also interesting is the larger decadal modulation of the 5–7-yr variance in PD, as demonstrated by its much larger 90% confidence intervals (Fig. 6). Given the fact that the change is not monotonic with CO_2 and that the PI/HC comparison yields insignificant results, changes to 5–7-yr variability are neglected for the majority of this analysis. However, some additional discussion may be found in section 7.

The probability distribution functions (PDFs) for Niño-3.4 scale-averaged wavelet power (SAWP) are shown in Figs. 6c,d for the 2–4- and 5–7-yr bands. Here SAWP is calculated following Torrence and Compo (1998):

$$\mathrm{SAWP} = \frac{\delta j \delta t}{C_\delta} \sum_{j=j_1}^{j_2} \frac{|W_n(s_j)|^2}{s_j}. \qquad (4)$$

Changes to the PDF shape are visible in both bands: this shows up as a positive result when a Kolmogorov–Smirnov (K–S) test is applied (not pictured). However, the K–S test can only measure changes to the distribution,

[2] All bandpassing was conducted using a tenth-order Butterworth filter; filter start and endpoints correspond to the −3-dB half-power interval boundaries.

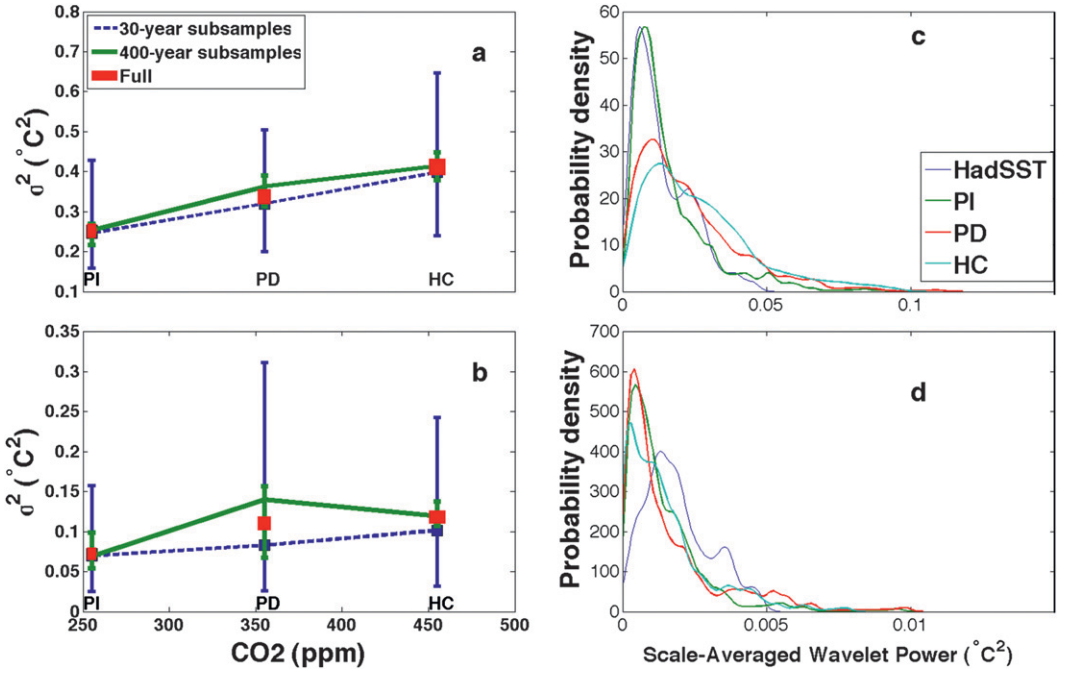

FIG. 6. Illustration of the significance of differences between CCSM3.5 simulations. (a),(b) Niño-3 SST variance subsampled at 30-yr (blue dashed line) and 400-yr (green solid line) intervals. (c),(d) PDFs of scale-averaged wavelet power. A (a),(c) 2–4-yr and (b),(d) 5–7-yr bandpass filter is used. Bandpass filters used are tenth-order Butterworth filters, and filter endpoints specified as the −3-dB half-power points.

not whether those changes could have arisen from internal ENSO variations. As shown by Stevenson et al. (2012), the K–S test yields significant differences even between ensemble members, making a less sensitive test essential.

The statistical significance of differences between model Niño-3.4 spectra is identified using the wavelet probability analysis (WPA) toolkit developed by Stevenson et al. (2010) and available online (http://atoc.colorado.edu/~slsteven/wpi/). The idea behind WPA is that if a single process is responsible for generating two time series, then their wavelet power PDFs should be roughly the same. Constructing wavelet PDFs from subsamples of a time series then creates a measure of natural variability: the degree to which PDFs of subintervals overlap indicates the expected internal scatter (Stevenson et al. 2010). The significance of differences between two time series may then be measured via hypothesis testing: the spectral overlap between the wavelet decomposition of a reference time series [here Niño-3.4 from the Second Hadley Centre Sea Surface Temperature (HadSST2) dataset of Rayner et al. (2006)] and that from the CCSM3.5 runs is computed, and the resulting distributions compared. The significance level at which the confidence intervals on the distributions overlap is then the minimum significance at which they differ. Full details of the procedure are available in Stevenson et al. (2010).

Results from WPA testing are shown in Table 2, calculated using a Morlet wavelet at a subsampling length of 250 yr. Here the numerical convention is to provide the significance of differences between simulations, where a change significant at the 90% level has a test value of 0.9. These results are consistent with the variance plots in Fig. 6: Niño-3 SST variability is significantly stronger in the 2–4-yr band in HC relative to PI. It

TABLE 2. Significance of differences in Niño-3 and Niño-4 spectral power between the CCSM3.5 simulations. Values are calculated using the WPA toolbox of Stevenson et al. (2010) and presented using a "1 − p" convention. A p value of 0.1 indicates 90% confidence that spectra differ and is reported as a value of 0.9 or greater. Entries less than 0.9 indicate that spectra are indistinguishable at 90% significance. All calculations use the Morlet wavelet and subsampling length of 250 yr.

Comparison	Niño-3	Niño-4
PI/PD 2–4 yr	0.90	0.45
PD/HC 2–4 yr	0.49	0.35
PI/HC 2–4 yr	1.00	0.02
PI/PD 5–7 yr	0.46	0.93
PD/HC 5–7 yr	0.43	0.72
PI/HC 5–7 yr	0.02	0.48

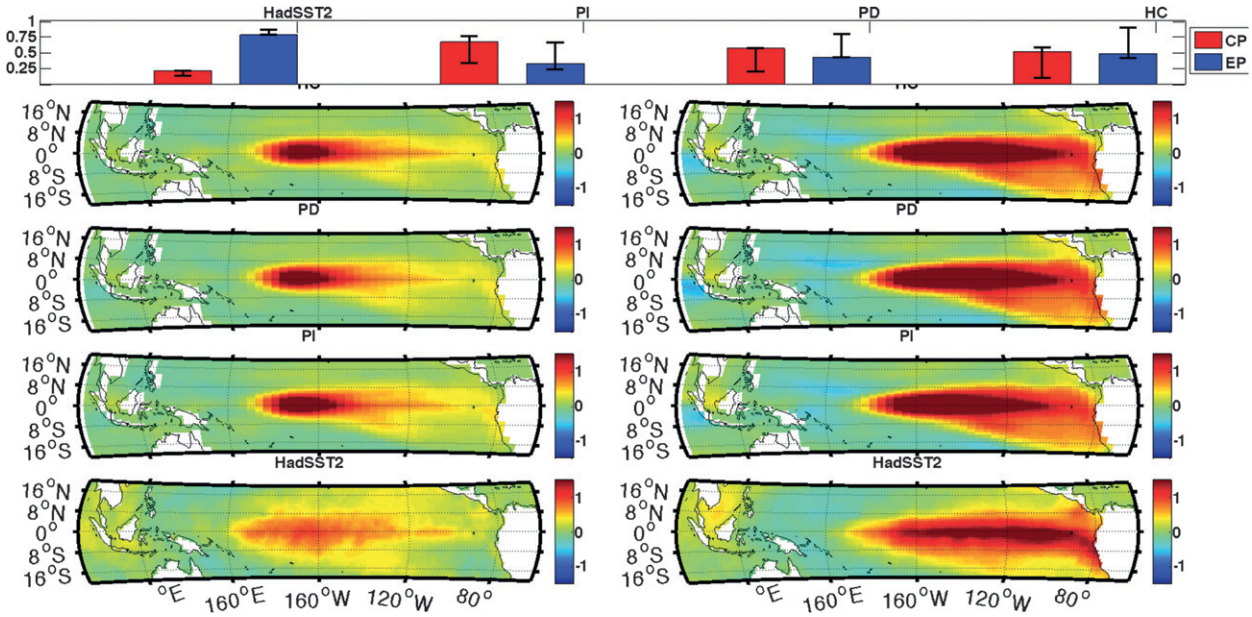

FIG. 7. EP and CP events in the CCSM3.5 simulations. Here the Yeh et al. (2009) definition is used, where El Niños having NDJ Niño-3 SST anomalies greater than (less than) Niño-4 SST anomalies are categorized as EP (CP). (top) Proportion of EP/CP El Niño events in observations and all CCSM3.5 simulations; EP events are shown in blue, CP in red. Error bars indicate the 90% bootstrap confidence interval, calculated by selecting 100-yr periods at random from PI, PD, and HC. Composite (left) CP and (right) EP SST anomaly patterns for (second row) PI, (third row) PD, (fourth row) HC, and (bottom) HadSST2.

should be noted that although the overall shift in Niño-3 2–4-yr power is toward stronger variability with CO_2, the change between PD and HC is insignificant. At longer periods (5–7-yr band), Niño-3 variability is statistically identical between all simulations, as is the case with Niño-4 2–4-yr variability. This provides additional justification for the exclusion of the 5–7-yr-period range from further analysis.

Finally, changes to the relative frequencies of central Pacific (CP or ''Modoki''; Ashok et al. 2007) and EP El Niño events are discussed, as this is a topic of considerable interest in the literature (Yu and Kao 2007; Kao and Yu 2009). It has been speculated that CP El Niño events have increased in frequency relative to EP events, based on changes that took place near the end of the twentieth century (Yeh et al. 2009). However, natural variability in ENSO ''flavors'' has since been shown to be substantial (Yeh et al. 2011) and some authors have concluded that twentieth-century variations in event types are consistent with multivariate red noise (Newman et al. 2011).

The distinction between event types is not a primary focus of this work, as the goal is to understand overall dynamical changes. That said, a preliminary investigation of the occurrence of CP and EP types of El Niño has been conducted and is presented in Fig. 7. Here, for simplicity, the definition of Yeh et al. (2009) has been followed, where CP and EP events are defined as El Niño periods [October–February (ONDJF) SST anomaly (SSTA) $\geq 0.7\sigma$] where the Niño-4/Niño-3 SST anomalies are larger, respectively. The anomaly time series were detrended prior to performing the calculation, and the resulting identification of CP/EP events in HadSST2 (Fig. 7) yields a list nearly identical to Yeh et al. (2009) (not pictured).

CCSM3.5 appears to have too many CP events relative to observations, possibly as a result of the ENSO ''center of action'' being too far west in the model (Deser et al. 2012). Figure 7 also shows that CP events decrease sharply in relative frequency with CO_2. In PI, CP events outnumber EP events by a factor of 2:1; the proportions are roughly equivalent in HC. However, the error bars in each are large, indicating that the changes may potentially be consistent with natural variability. If this increase can be shown to be robust, the most likely explanations would be the overall increase in equatorial stratification and the enhancement of equatorial Kelvin wave activity with CO_2 (see section 6), which should favor EP events.

These CCSM3.5 results should serve as a cautionary tale for drawing conclusions regarding future changes to El Niño types using short simulations, and we recommend that similar analyses be performed with other models to determine the robustness of this result.

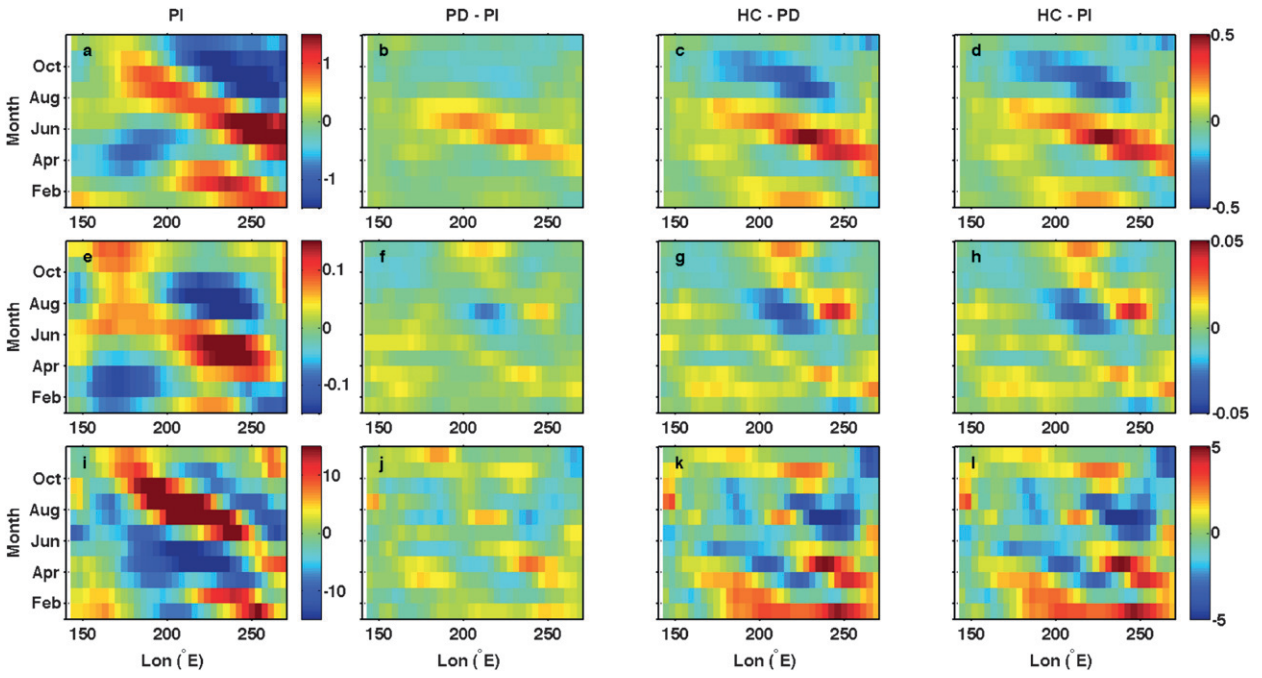

FIG. 8. Annual cycle in the equatorial Pacific, averaged over 1°S–1°N: (a)–(d) SST (°C), (e)–(h) zonal wind stress (N m^{-2}), and (i)–(l) latent heat flux (W m^{-2}). Columns show values for (a),(e),(i) PI; (b),(f),(j) PD − PI; (c),(g),(k) HC − PD; and (d),(h),(l) HC − PI.

5. Annual cycle response

The phase locking of ENSO to the annual cycle has been documented in many studies, and indeed was one of the earliest observed features of the oscillation (Rasmusson and Carpenter 1982). Paradigms for understanding the ENSO–annual cycle interaction include chaotic coupling (Jin et al. 1994) and seasonally variable ocean stability altering the amplification of ENSO-related anomalies (Tziperman et al. 1997). Recent work also indicates the role of seasonal variations in wind stress on El Niño termination (McGregor et al. 2012).

Despite the importance of the annual cycle to ENSO, the influence of climate change on the annual cycle of SST is poorly understood, and relatively little attention has been paid to this question to date. One exception is the hypothesis of Timmermann et al. (2004), which states that the differential land–sea heating that results from climate change leads to an equatorial meridional wind stress anomaly, which in turn creates an amplification of the seasonal cycle through unstable wind–evaporation–SST feedback. The mean changes in land and ocean temperatures were discussed in section 3; the temperature contrast and meridional wind stress are clearly visible in Fig. 4, consistent with the Timmermann et al. (2004) hypothesis.

The second part of the hypothesis is that unstable air–sea coupling drives a westward-propagating SST anomaly along the equator, accompanied by a Gill-type zonal wind stress response (easterly to the east and westerly to the west of the SST anomaly). This is precisely what is observed in CCSM3.5, as shown in Figs. 8a–h. There, the difference plots between PD-PI and HC-PD show a positive SST anomaly forming during boreal spring/summer and propagating to the west, with wind stress anomalies of the appropriate sign on either side. The latent heat flux anomalies (Figs. 8i–l) are also consistent with westward-propagating instabilities associated with cloud feedbacks; thus, while not conclusively establishing causality, the results of Fig. 8 provide strong circumstantial evidence that the annual cycle increase could be caused by such a mechanism.

The fact that the increase in annual cycle amplitude accompanies an increase in interannual variability seems at odds with previous work indicating an inverse relationship (An et al. 2010); this was hypothesized to result from a westward shift in the equatorial Pacific convective center, which led to a more rapid reflection of the Rossby wave signal off the western boundary and subsequent termination of El Niño. A stronger annual cycle was also associated with weaker vertical stratification, weaker air–sea coupling strength, and therefore weaker ENSO amplitude. In the CCSM3.5 simulations, higher CO_2 is associated with an eastward shift of the convective center and stronger vertical stratification (see section 3); this may potentially compensate for the

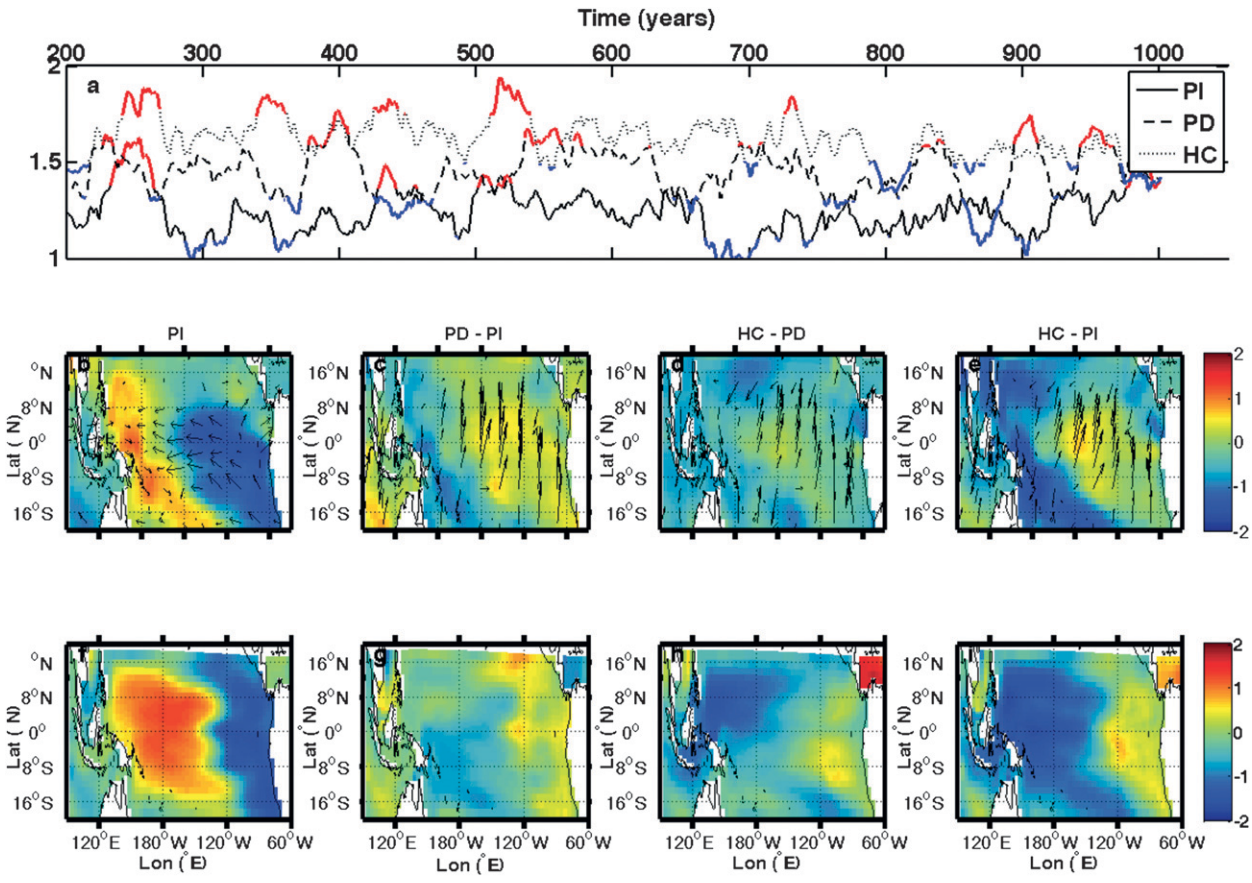

FIG. 9. Composite difference maps of SST, wind stress, and equatorial temperature for periods with strong vs weak annual cycle amplitudes. (a) Time series of Niño-3.4 wavelet spectral power in the annual cycle (averaged from 0.75 to 1.25-yr periods) for PI (solid), PD (dashed), and HC (dotted). Epochs (15-yr running-mean values) having an annual cycle greater (less) than 1σ from the mean are indicated by red (blue) shading on the appropriate time series. The composite differences between strong and weak epochs are shown for (b)–(e) SST (colors)/wind stress (arrows) and (f)–(i) thermocline depth: (b),(f) PI; (c),(g) PD − PI; (d),(h) HC − PD in (d); and (e),(i) HC − PI.

influence of the annual cycle and cause the difference between these results and those of An et al. (2010). Initial confirmation of this hypothesis is provided in Fig. 9, which shows the changes between JJA and DJF in SST, wind stress, and thermocline depth for epochs in each simulation having stronger or weaker annual cycle amplitudes. As in An et al. (2010), epochs with a stronger annual cycle show a deepened central Pacific thermocline (Fig. 9f), a warmer western Pacific, and enhanced trade winds (Fig. 9b). These changes are all opposed by the tendencies with higher CO_2 (Figs. 9c–e, g–l), which tend to suppress the effect of the annual cycle on the mean state.

The magnitude of the annual cycle in SST is not the only metric previously examined in the literature, and indeed the proportion of energy in the annual cycle has been cited as important for ENSO amplitude (Guilyardi 2006). This is examined in Figs. 5c,d, where the proportion of wavelet spectral power between 9- and 15-month periods is shown. The 1σ confidence intervals overlap in Niño-3 for PI/PD and PD/HC, but a clear tendency toward a proportional weakening of the annual cycle is observed. The trend is even stronger in the western Pacific (Niño-4 SST; Fig. 5d). This is not discussed in detail here, but as will be shown in section 6, the proportional weakening of the annual cycle may represent an increase in the ability of seasonal changes to excite interannual variability.

6. Changes to interannual variability

The dynamics of the 2–4-yr variability is next examined, in both the atmosphere and ocean. Figure 10 shows thermocline, SST, and subsurface temperature variability calculated using the standard deviation of the 2–4-yr bandpassed time series. In Figs. 10a–c, the SST standard deviation pattern exhibits the canonical ''horseshoe'' El Niño pattern. This pattern is visible in all three simulations,

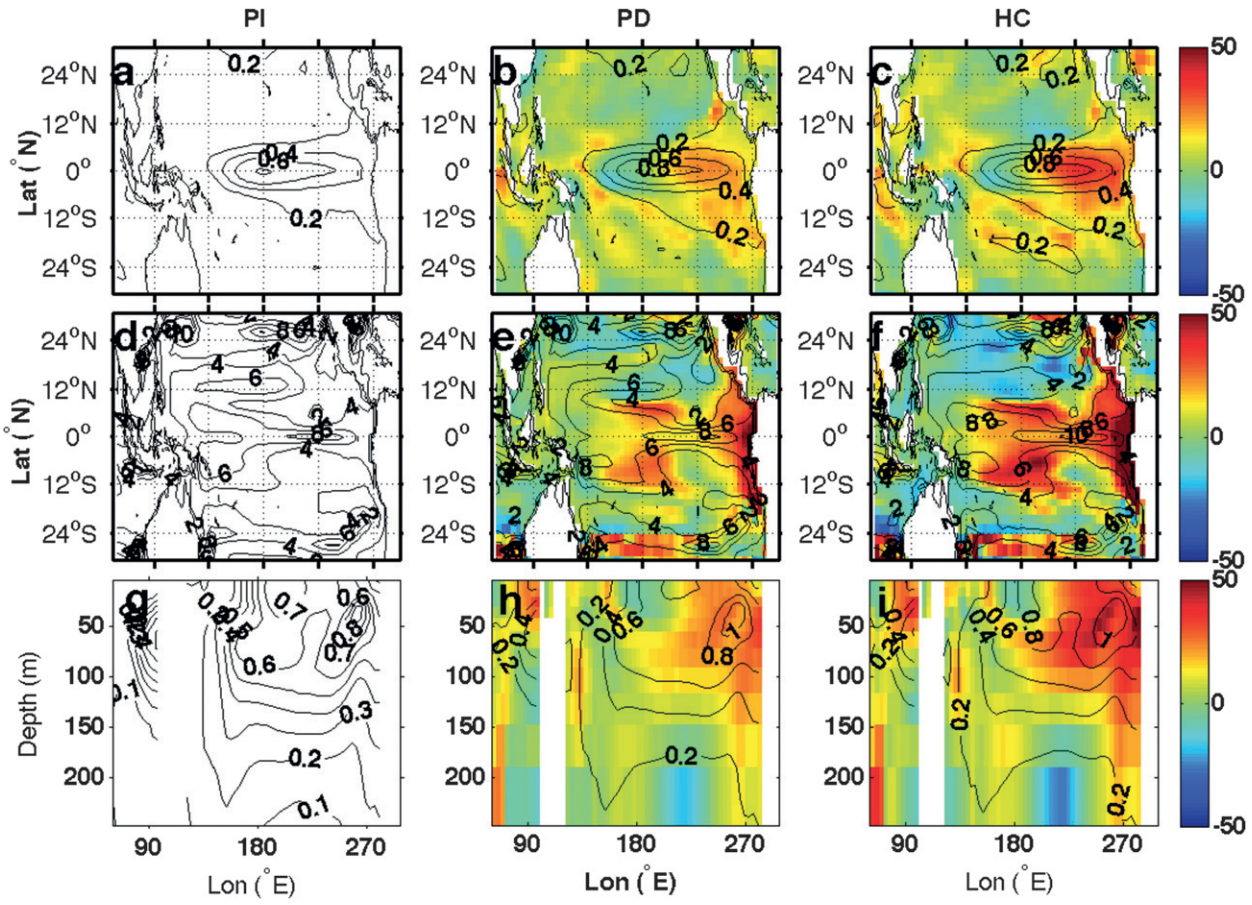

FIG. 10. Oceanic variability (bandpass filtered with −3-dB points at 2 and 4 yr), showing variance of (a)–(c) SST (°C^2), (d)–(f) thermocline depth (m^2), and (g)–(i) subsurface temperature (°C^2). Shading in the middle and right columns represents the percentage change from PI.

and is enhanced at higher CO_2. Changes between HC and PI are on the order of 100% in the eastern Pacific, consistent with the Niño-3 spectral results of section 4. A decrease in 2–4-yr variability is seen in the western Pacific. Taken together, these changes indicate an overall eastward shift of the ENSO-related SST variability.

Thermocline variability is shown in Figs. 10d–f. Variations bearing a strong resemblance to Kelvin waves strengthen along the equator at higher CO_2, and off the equator there are signals observed near 10°N/S, latitudes favored for the generation of Rossby waves (Capotondi et al. 2003). In HC, the variability near 10°N decreases in HC relative to PI, while that at 10°S strengthens. This may be interpreted as an enhancement/weakening of Rossby waves in the Southern/Northern Hemispheres. It should also be noted that these locations are also the sites of corresponding changes in SST variability (Figs. 10a–c).

Figures 10g–i show the standard deviation of mean temperature over 2°S–2°N, as a function of depth. Enhanced variability is seen both at the surface and at depth. A closer examination of Figs. 10g–i reveals that there are several distinct ''centers'' of large variance rather than a uniform region of variability, all of which strengthen with CO_2. The subsurface SST variability near 100–150 m is most likely a simple consequence of variability involving the main thermocline, and Figs. 10g–i show changes over the same range of longitudes where enhanced equatorial thermocline variability is observed in Figs. 10e,f. Likewise, the surface variability in the eastern equatorial Pacific seems to be a straightforward consequence of the arrival of Kelvin waves at the eastern boundary, creating a reduction in upwelling.

The picture provided by Fig. 10 is consistent to first order with the delayed oscillator of Zebiak and Cane (1987) and Battisti and Hirst (1989), in which Kelvin and Rossby wave dynamics generate the majority of the SST signal. In such a scenario it is possible that the increased equatorial stratification and resulting enhancement in

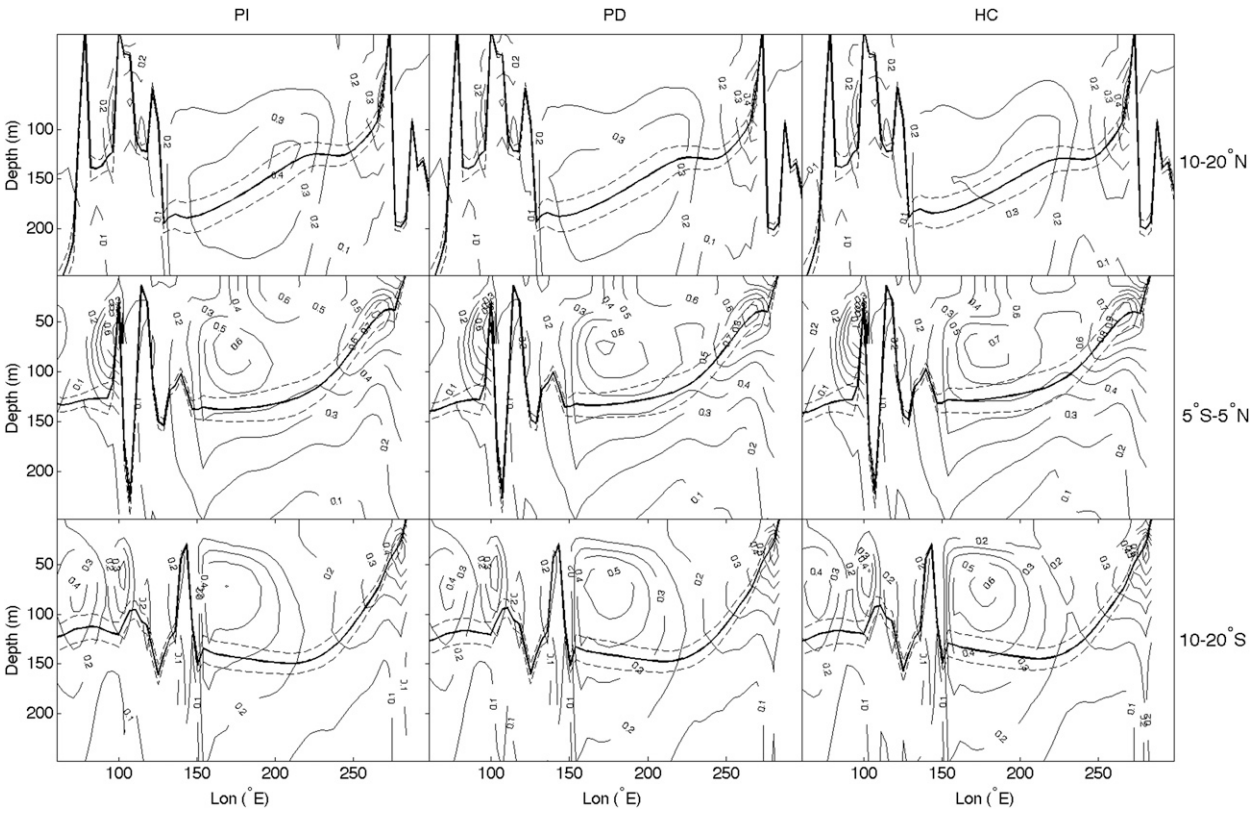

FIG. 11. Variability in subsurface ocean temperature (variance of gridpoint time series, bandpass filtered with −3-dB points at 2 and 4 yr). Thick solid lines indicate the mean position of the thermocline; dashed lines show the $\pm 1\sigma$ uncertainty of the mean thermocline position.

SST variability could provide the entire explanation for enhanced ENSO amplitude. Such an increase in oscillator activity could potentially be tied to an increase in the stochastic forcing due to westerly wind bursts (WWBs; Gebbie et al. 2007). However, there still remains the question of hemispheric asymmetry. The thermocline standard deviation maps in Figs. 10d–f show that the Rossby wave signature grows stronger (weaker) in the Southern (Northern) Hemisphere—this is again borne out in subsurface temperature variability and is not readily explained by a simple oscillator model. Figure 11 shows similar standard deviation maps equivalent to those in Figs. 10g–i, averaged over 10°–20°S, 5°S–5°N, and 10°–20°N: overall subsurface temperature variability strengthens in southern latitudes and weakens in northern latitudes.

A hemispherically asymmetric mechanism is required to explain the asymmetric subsurface variability changes; the most likely candidate for a hemispherically asymmetric forcing is the seasonal cycle. Section 5 demonstrated that the seasonal cycle of SST changes drastically with CO_2 in these simulations, which should in turn affect ENSO (Alexander et al. 2002; Jin et al. 1994; Xie 1996). Thus, seasonal composites of SST and wind stress during various phases of El Niño are shown in Fig. 12. Hemispherically asymmetric changes are indeed seen in Fig. 12, with the most dramatic SST signatures at 9–12 months after the peak El Niño. There a cooling is seen that stretches from the eastern to central Pacific, suggesting that subtropical signals may affect the termination of El Niño events in CCSM.

The preceding analysis suggests that changes to the seasonal cycle may be responsible for the hemispherically asymmetric response of ENSO to CO_2 increases; such a hypothesis is physically plausible. In the Northern Hemisphere, climatological convergence in wind stress is associated with a mean thermocline deepening near 10°N in the eastern Pacific. In the corresponding Southern Hemisphere location, the reverse occurs; climatological divergence leads to a thermocline shoaling. These changes should make the system less sensitive to seasonal changes in the winds in the Northern Hemisphere and more sensitive to those in the Southern Hemisphere. Additionally, the magnitude of seasonal changes to off-equatorial convergence/divergence increases with CO_2 (not pictured) in both hemispheres.

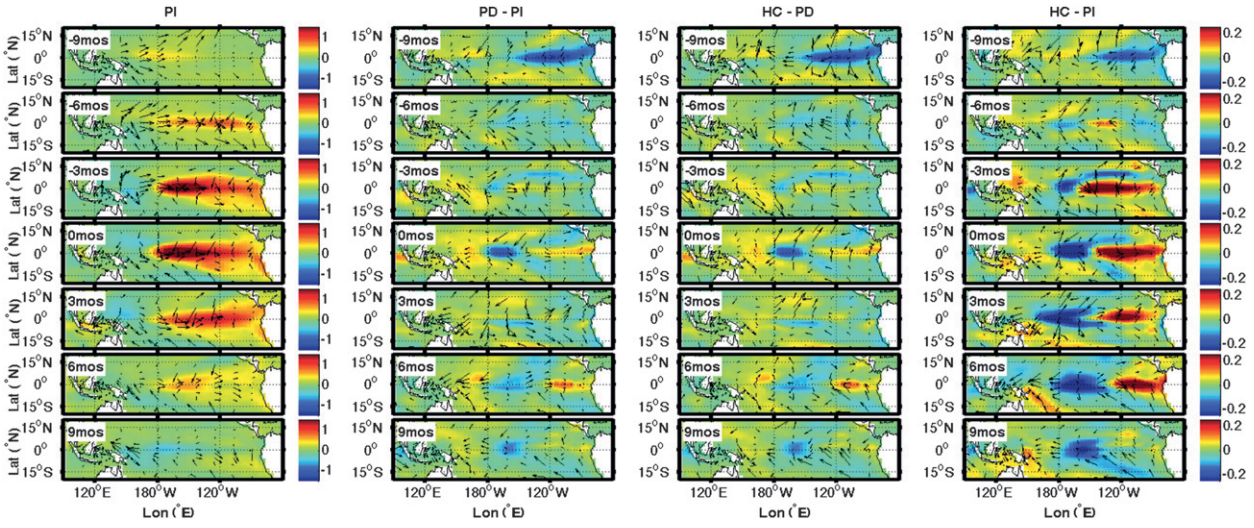

FIG. 12. Composites of SST (colors) and wind stress (arrows) at various phases of El Niño. Here El Niño events are defined as periods where the Niño-3.4 SST anomaly exceeds 1σ during DJF; offsets from the DJF El Niño anomaly are given in months. SST and wind stress composites are calculated over a 3-month period centered about the time indicated.

This is physically consistent with the changes to variability observed in Fig. 10.

Numerous studies (Vimont et al. 2003; Alexander et al. 2002, 2010) have shown that North Pacific heat flux anomalies may lead to the development of either El Niño or La Niña events. This mechanism is shown to operate in CCSM3.5, following Vimont et al. (2003) in applying a singular value decomposition (SVD) analysis to SST and zonal wind stress; τ_x is averaged over May–September (MJJAS) during year 1, and SST over November–March (NDJFM) the following winter (years 1–2). The SST during NDJFM from the previous winter (years 0–1), averaged over 6°S–6°N, 180°–90°W, is linearly removed from both fields, and the first principal component (PC1) is then calculated for each pair of fields.

The regression patterns for SST and τ_x on PC1 described above are shown in Fig. 13. Only latitudes equatorward of 40° are plotted, to highlight the subtropical portion of the seasonal footprinting mechanism (SFM); SST anomalies propagate from the eastern subtropical Pacific down into the tropics (Fig. 13, top row), where they induce the weakening of the equatorial trade winds (Fig. 13, middle row) accompanying the development of an El Niño event. The propagation of subtropical SST anomalies into the tropics is confirmed by regressing the summertime (MJJAS) SST pattern onto PC1 for SST/sea level pressure, as in Vimont et al. (2003) (Fig. 13, bottom row). Comparing PI, PD, and HC then reveals that there is a tendency for the subtropical SST pattern to shift to the south with CO_2, consistent with the enhanced climatological convergence in the region. The regression also weakens in the central Pacific near 10°–15°N, 160°E, indicating that the Northern Hemisphere seasonal forcing becomes less efficient at exciting El Niño events at higher CO_2.

Next, changes in the Southern Hemisphere are examined. The seasonality of the fields chosen for the SVD has been altered to reflect the differences in the generation of the propagating signal. To capture the maximum climatological divergence in the Southern Hemisphere subtropics, τ_x is averaged over JAS (year 1; not pictured). The averaging period for SST is taken as March–May (MAM) of the following year (year 2). As in Fig. 13, the NDJFM central Pacific SST from the winter of years 0–1 is linearly subtracted from both fields prior to performing the SVD. Results are shown in Fig. 14: patterns similar to those in Fig. 13 emerge, with westerly wind anomalies seen along the equator (Fig. 14, middle row).

The subtropical signal in Fig. 14 is more complex than its Northern Hemisphere counterpart, and the generation of the signal is not strictly analogous to that in Fig. 13. The middle row of Fig. 14 shows that near 12°S, easterly anomalies dominate in the western/central Pacific and westerly anomalies in the eastern; thus a net divergence is present, which strengthens from PI to HC. The area of maximum divergence, furthermore, is collocated with a cold anomaly in SST. The regression of NDJ SST onto the SST/τ_x PC1 shown in the bottom row of Fig. 14 then shows a tendency for propagation of the cold anomaly toward the equator, consistent with the composites shown in Fig. 12. Finally and most importantly, comparison of the bottom panels of Fig. 14 clearly

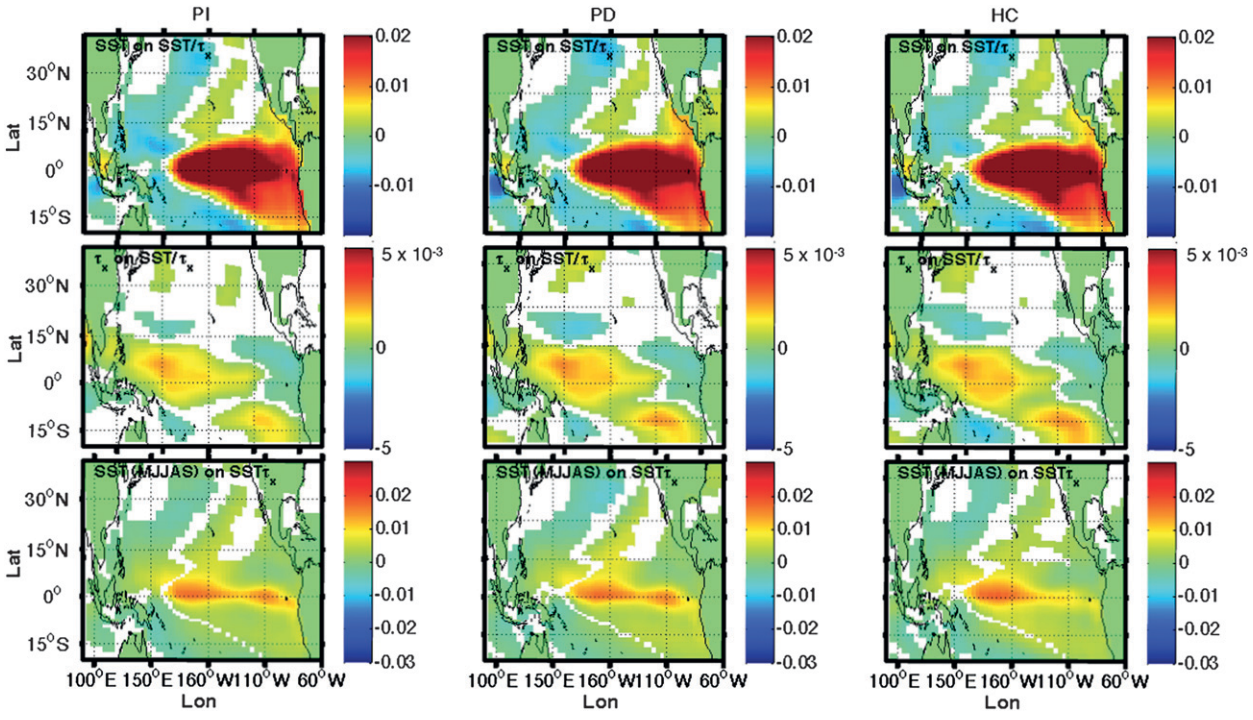

FIG. 13. SFM in CCSM3.5. The SVD analysis of Vimont et al. (2003) has been reproduced for (left) PI, (middle) PD, and (right) HC. Zonal wind stress has been averaged over MJJAS (year 1), and SST over NDJFM the following winter (year 1). (top), (middle) Regressions of SST and τ_x on the SST/τ_x PC1. (bottom) Regression pattern for SST during MJJAS of year 1 on the SST/τ_x PC1, to illustrate changes in the efficiency of this pattern at generating a propagating SST signal.

shows that the subtropical SST signal strengthens from PI to HC. Although not conclusive in and of itself, this is preliminary evidence that seasonally dependent changes in the wind stress divergence can lead to propagating signals that are enhanced in the Southern Hemisphere at higher CO_2, consistent with the results presented in earlier sections.

7. Long-period variability

In all of the previous analyses, the variability at periods longer than 5 yr was neglected. This was done since the amplitude of variability does not change significantly with CO_2, but the lack of signal is itself an interesting result. As in section 6, the bandpass-filtered variability is presented for SST, thermocline depth, and subsurface temperature in Fig. 15. Here the −3-dB points of the filter are located at 5–7 yr. The changes to SST variability are largest in the far eastern Pacific, and the western Pacific signals near 10°N/S observed in the 2–4-yr band are absent. This likely indicates that the Rossby/Kelvin wave dynamics are not active at these frequencies. However, there is a peak in variability near 10°N in the central Pacific; this may relate to remote influences on the ITCZ, which could manifest on decadal time scales. The remaining equatorial signal in the eastern Pacific is likely a simple consequence of the increased stratification and shoaling of the mixed layer.

8. Preliminary comparison with CCSM4: Implications for CMIP

ENSO is highly sensitive to changes in model physics (Guilyardi 2006; Philip and van Oldenborgh 2006), meaning that any single-model result is not conclusive in and of itself. Unfortunately, there are very few model experiments that permit the robust detection of dynamical changes in GCMs; for example, CMIP5 does not include stabilized, high-CO_2 integrations long enough to provide stable ENSO statistics (Taylor et al. 2012).

An illustration of the need for long stabilized simulations with additional CMIP-class models is provided, using the CCSM4 1° representative concentration pathway (RCP) ''extension'' simulations for 2100–2300 (Meinshausen et al. 2011) as a rough comparison case. The extension simulations are the closest available equivalents to a high-CO_2 control, being stabilization scenarios from 2100 to 2300 for each of the twenty-first-century projection suites. One of the midrange extension runs, RCP4.5 (or RCP4.5E), is adopted as a

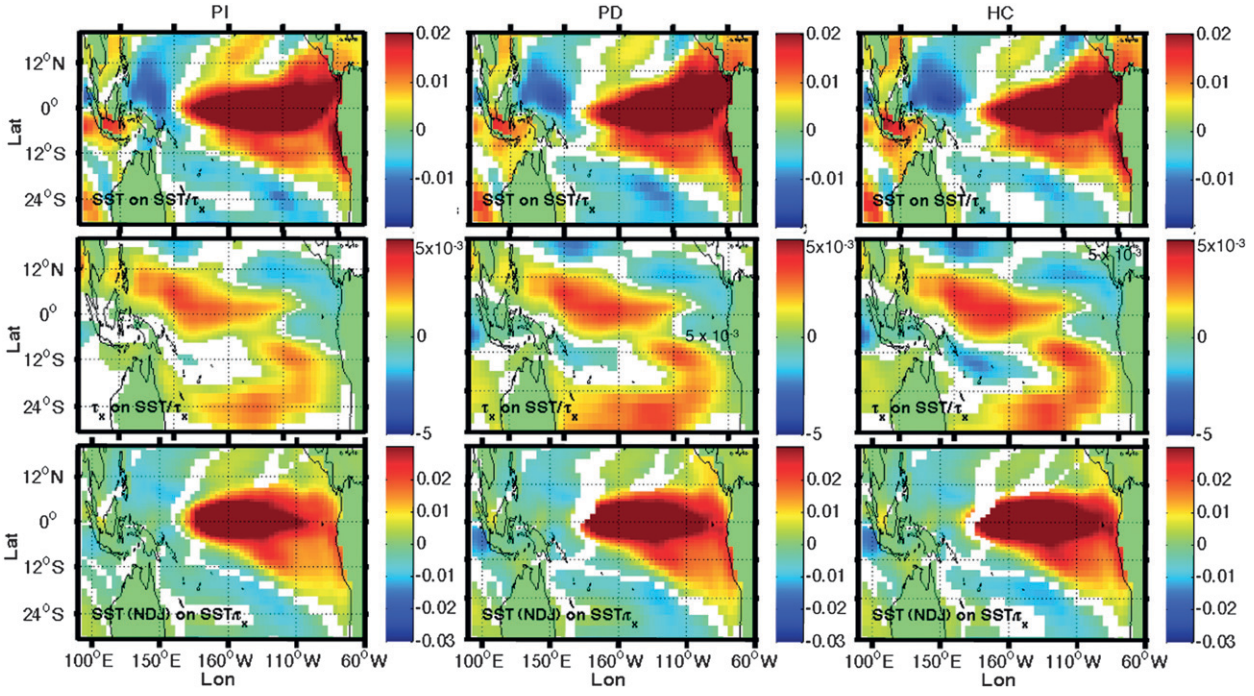

FIG. 14. SH "equivalent" to the SFM in CCSM3.5. Zonal wind stress has been averaged over JAS (year 1), and SST over MAM the following spring (year 2). SST during NDJFM of the previous winter (year 0) was linearly subtracted from both fields prior to performing the SVD. (top),(middle) Regressions of SST and τ_x on PC1 for SST/τ_x (bottom) Regression pattern for SST during NDJ of years 1–2 on PC1 for SST/τ_x, to illustrate changes in the efficiency of this pattern at generating a propagating SST signal.

representative example to illustrate potential ENSO-relevant differences: here, only the last 50 yr are used (A.D. 2250–99) to minimize ramp-up effects.

The mean-state response of CCSM4 to CO_2 increases was documented by Stevenson et al. (2012) and is qualitatively similar to that of the T31 × 3 CCSM3.5. The equatorial zonal SST gradient and trade winds decrease, ocean stratification increases, and the Walker circulation shifts eastward. Yet the ENSO amplitude response appears quite different; the changes between CCSM3.5 and CCSM4 clearly impact the ENSO climate sensitivity, but how?

The most obvious difference between the two model versions is resolution, which increases threefold between the CCSM3.5 T31 × 3 and CCSM4 1° configurations. This in turn has a dramatic impact on convection and therefore on the level of westerly wind burst activity in the model (Jochum et al. 2009; Neale et al. 2012, manuscript submitted to *J. Climate*). WWBs are weak in the T31 × 3 configuration of the CCSM3.5 (Fig. 16), which is reflected in the smaller absolute magnitudes of $\sigma^2\tau_x$ along the equator in Fig. 16a relative to Fig. 16c. This may potentially be a significant model bias, since WWBs are known to initiate ENSO activity in the real world (Harrison and Vecchi 1997; McPhaden 2004; Lengaigne et al. 2004). To evaluate changes to high-frequency wind stress variability, the submonthly zonal wind stress variance is mapped over the tropical Pacific (Fig. 16). The submonthly variance was chosen as a computationally inexpensive method of measuring the combined influences of WWBs (which take place a few times per year and last 5–20 days; Harrison and Vecchi 1997), synoptic weather activity, and the Madden–Julian oscillation (MJO; Madden and Julian 1994).

Figure 16 shows that the patterns of CO_2 response are clearly distinct between models; in particular, the western Pacific warm pool displays markedly different behavior between CCSM3.5 and CCSM4. In CCSM3.5, the total variance off the Papua New Guinea coast increases by roughly 20%, while a decrease occurs over the entire warm pool in CCSM4. This seems in conflict with previous studies (Gebbie et al. 2007), which find that WWB activity increases with warm pool temperature and longitudinal extent. Is this an indication that the MJO triggering of WWBs (and possibly, therefore, El Niño events) does not occur in CCSM4? If not, are there other competing processes that "damp out" the MJO influence on developing ENSO events? How are these processes represented in other climate models? The present study cannot answer these questions; however, Fig. 16 should serve as ample evidence for changes that affect the simulated convective influence on ENSO

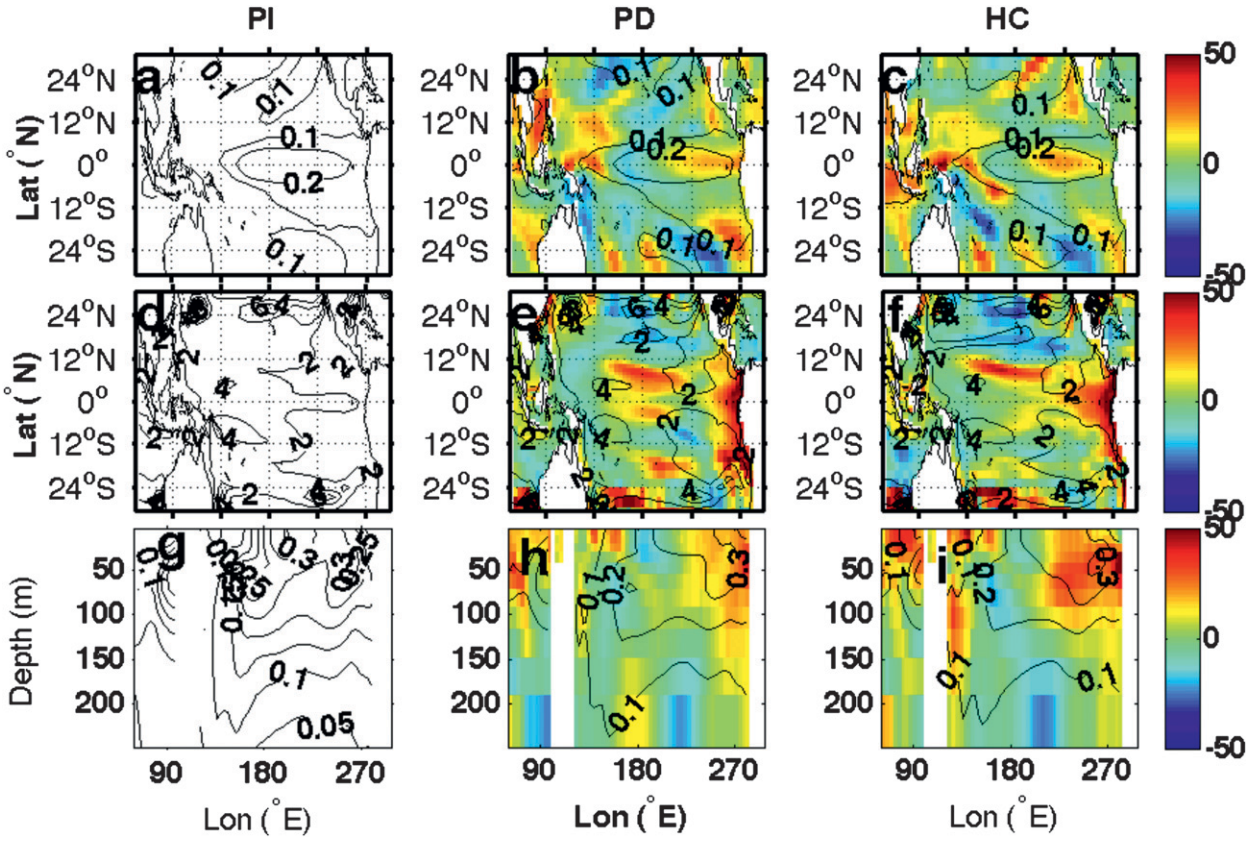

FIG. 15. As in Fig. 10, but with bandpass filtering performed over the 5–7-yr band.

within a single model family. It should also be noted that high-frequency wind stress variability is only a single example of ENSO-relevant dynamical changes between models; others doubtless exist.

A complete understanding of the dynamical sensitivities of ENSO with CO_2 in coupled general circulation models requires stabilized simulations at several different CO_2 levels, conducted with a wide variety of models. If CCSM can be considered representative in terms of ENSO CO_2 sensitivity (which, of course, has yet to be determined), then potentially one might not detect CO_2-induced ENSO changes unless an additional control at high CO_2 was run. However, it is clear that whatever the desired CO_2 level, quantifying changes to ENSO dynamics in a statistically robust manner requires multiple centuries at a stable forcing level, which should be considered during future model intercomparison efforts.

9. Conclusions

This study has provided the first millennial-scale look at ENSO–CO_2 linkages in equilibrated climate model simulations, relying primarily on three T31 × 3 CCSM3.5 simulations conducted at 255, 355, and 455 ppm CO_2 with otherwise identical model configurations. Changes to the atmosphere/ocean mean state with increased CO_2 are similar to those found in previous multimodel studies. Enhanced SST warming is seen in the eastern Pacific, reducing the zonal SST gradient. An overall weakening of the overturning circulations in the atmosphere and ocean is seen, consistent with the Vecchi and Soden (2007) and Held and Soden (2006) picture of a weakening boundary layer/free atmosphere exchange of moisture. In the atmosphere, the strongest circulation shift is seen during boreal summer, when the Hadley cell is at its northernmost position.

In the ocean, vertical thermal stratification increases with CO_2, most likely through a combination of increased surface heat flux, decreased equatorial upwelling, and reduced subtropical cell strength. The thermocline shoals accordingly, by a percentage remarkably consistent with the scaling relationship derived by Luyten et al. (1983) and presented in detail in Pedlosky (1996). This indicates that the major processes controlling the climatological mean thermocline depth are nondissipative: cross-isopycnal mixing may be neglected at equilibrium.

Changes to the SST seasonal cycle are substantial, with statistically significant strengthening occurring in

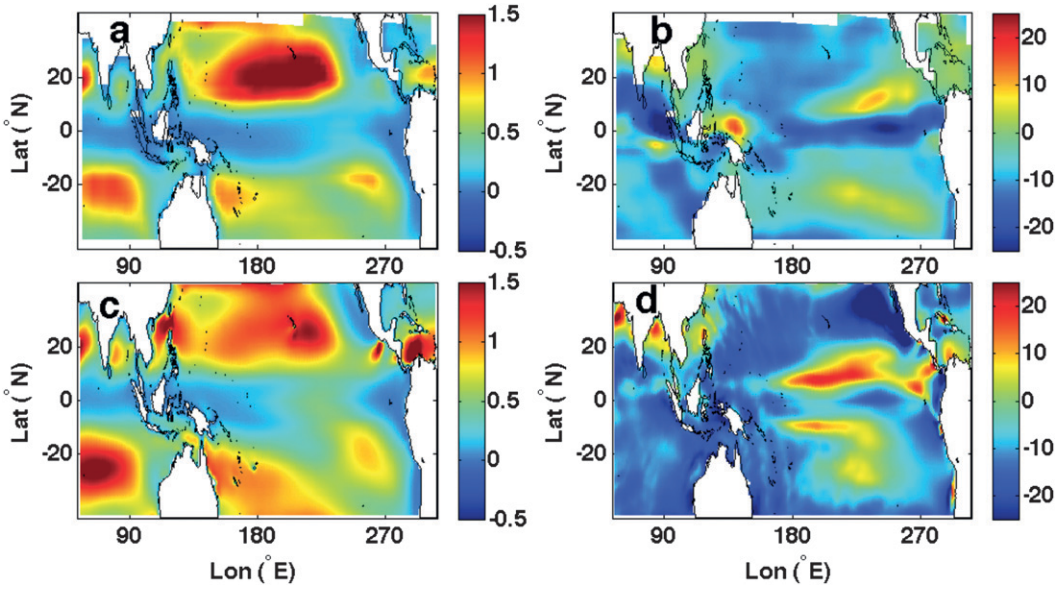

FIG. 16. Submonthly zonal wind stress variance (N^2 m^{-4}). (a) Mean variance for PI (CCSM3.5), years 200–1000. (b) Difference between HC and PI (CCSM3.5), years 200–1000 for both. (c) Mean variance for RCP4.5 (CCSM4), years 2250–99. (d) Difference between RCP4.5 and the CCSM4 1850 control (years 800–1299). Note that in (b),(d), the units are percent [given relative to PI for (b), CCSM4 1850 control for (d)].

both the Niño-3 and Niño-4 regions. The stronger seasonal cycle may arise from the increased land/sea temperature contrast. The influence of the seasonal cycle on ENSO appears to differ from the results of An et al. (2010), who showed that a stronger seasonality led to a deepening of the thermocline and westward shift of convective activity. These changes would tend to weaken air/sea coupling and lead to more rapid El Niño termination by reducing the time for Rossby wave reflection from the western boundary; however, the mean changes caused by CO_2 increases oppose those of the seasonal cycle in CCSM3.5.

The ratio of eastern Pacific (EP) to central Pacific (CP) El Niño events increases with CO_2, although internal variability is extremely large. It remains unclear whether this result is model dependent; however, these results suggest that it is at least possible that EP events might become more common in the future. EP El Niños are generally favored under conditions where thermocline variability dominates over surface-forced variations (Kao and Yu 2009); the enhanced vertical stratification with CO_2 in these simulations might therefore lead to more frequent EP events.

The ENSO-variance response to CO_2 in CCSM3.5 is a strengthening that is statistically significant at 2–4-yr periods only. In the 2–4-yr band, SST and thermocline variability are enhanced along the equator because of the increased stochastic triggering of ENSO events via equatorial Kelvin waves. Variability near 10°N weakens with CO_2, and a corresponding strengthening is seen near 10°S, locations where the mean thermocline deepens and shoals, respectively. Analysis of seasonally forced propagating signals then suggests that changes transmitted via the WES feedback may be responsible for the hemispherically asymmetric response.

Longer-period (5–7 yr) oscillations differ somewhat between simulations, with a slight tendency toward amplification with CO_2. The long-period (5–7 yr) variability is analyzed separately, as the changes with CO_2 are not statistically significant. The internal variability in this band also appears larger in PD than in either PI or HC. The causes for this variability are unclear but may potentially involve modulation of the ITCZ position on long time scales.

Intermodel differences are approximated by adopting the CMIP5 CCSM4 extension run for RCP4.5 as a comparison case to CCSM3.5. Substantial differences in the wind stress response to increased CO_2 are observed, although the mean-state response to CO_2 is the same in both models. A good illustration of model differences is the submonthly wind stress variability, which decreases with CO_2 over the western Pacific warm pool in CCSM4; stochastic ENSO forcing may be highly sensitive to the modeled atmospheric convection.

These results show that even within the same model family there are large differences in ENSO climate sensitivity. Millennial-scale integrations at varying CO_2 levels are necessary to ensure that sampling bias does not contaminate the results; this stands as a challenge to

the climate modeling community as a whole, and is an essential step toward understanding the controls on ENSO dynamics in future climates.

Acknowledgments. SS was supported by the NASA Earth & Space Science Fellowship (NESSF NNXO9AO20H) for much of this work. BFK is supported by NSF FRG0855010. MJ is supported by NSF through NCAR. This research used computing resources of the Climate Simulation Laboratory at NCAR. The suggestions of two anonymous reviewers led to significant improvements to the manuscript. We also acknowledge A. Capotondi, W. Han, and A. Timmermann for helpful discussions during the course of this research.

REFERENCES

AchutaRao, K., and K. R. Sperber, 2006: ENSO simulation in coupled ocean-atmosphere models: Are the current models better? *Climate Dyn.,* **27,** 1–15.

Alexander, M. A., I. Bladé, M. Newman, J. R. Lanzante, N.-C. Lau, and J. D. Scott, 2002: The atmospheric bridge: The influence of ENSO teleconnections on air–sea interaction over the global oceans. *J. Climate,* **15,** 2205–2231.

——, D. J. Vimont, P. Chang, and J. D. Scott, 2010: The impact of extratropical atmospheric variability on ENSO: Testing the seasonal footprinting mechanism using coupled model experiments. *J. Climate,* **23,** 2885–2901.

An, S.-I., Y.-G. Ham, J.-S. Kug, A. Timmermann, J. Choi, and I.-S. Kang, 2010: The inverse effect of annual-mean state and annual-cycle changes on ENSO. *J. Climate,* **23,** 1095–1110.

Ashok, K., S. Behera, A. Rao, H. Weng, and T. Yamagata, 2007: El Niño Modoki and its teleconnection. *J. Geophys. Res.,* **112,** C11007, doi:10.1029/2006JC003798.

Battisti, D. S., and A. C. Hirst, 1989: Interannual variability in a tropical atmosphere–ocean model: Influence of the basic state, ocean geometry and nonlinearity. *J. Atmos. Sci.,* **46,** 1687–1712.

Capotondi, A., M. Alexander, and C. Deser, 2003: Why are there Rossby wave maxima in the Pacific at 10°S and 13°N? *J. Phys. Oceanogr.,* **33,** 1549–1563.

Collins, M., and Coauthors, 2010: The impact of global warming on the tropical Pacific Ocean and El Niño. *Nat. Geosci.,* **3,** 391–397, doi:10.1038/NGEO868.

Danabasoglu, G., and J. Marshall, 2007: Effects of vertical variations of thickness diffusivity in an ocean general circulation model. *Ocean Modell.,* **18,** 122–141.

Deser, C., and Coauthors, 2012: ENSO and Pacific decadal variability in the Community Climate System Model version 4. *J. Climate,* **25,** 2622–2651.

Döös, K., and J. Nilsson, 2011: Analysis of the meridional energy transport by atmospheric overturning circulations. *J. Atmos. Sci.,* **68,** 1806–1820.

Fedorov, A. V., and S. G. Philander, 2000: Is El Niño changing? *Science,* **288,** 1997–2002.

——, and ——, 2001: A stability analysis of tropical ocean–atmosphere interactions: Bridging measurements and theory for El Niño. *J. Climate,* **14,** 3086–3101.

Gebbie, G., I. Eisenman, A. Wittenberg, and E. Tziperman, 2007: Modulation of westerly wind bursts by sea surface temperature: A semi-stochastic feedback for ENSO. *J. Atmos. Sci.,* **64,** 3281–3295.

Guilyardi, E., 2006: El Niño–mean state–seasonal cycle interactions in a multi-model ensemble. *Climate Dyn.,* **26,** 329–348.

Harrison, D. E., and G. A. Vecchi, 1997: Westerly wind events in the tropical Pacific, 1986–95. *J. Climate,* **10,** 3131–3156.

Held, I., and B. Soden, 2006: Robust responses of the hydrological cycle to global warming. *J. Climate,* **19,** 5686–5699.

Jin, F.-F., J. D. Neelin, and M. Ghil, 1994: El Niño on the devil's staircase: Annual subharmonic steps to chaos. *Science,* **264,** 70–72.

Jochum, M., 2009: Impact of latitudinal variations in vertical diffusivity on climate simulations. *J. Geophys. Res.,* **114,** C01010, doi:10.1029/2008JC005030.

——, G. Danabasoglu, M. Holland, Y.-O. Kwon, and W. G. Large, 2008: Ocean viscosity and climate. *J. Geophys. Res.,* **113,** C06017, doi:10.1029/2007JC004515.

——, B. Fox-Kemper, P. H. Molnar, and C. Shields, 2009: Differences in the Indonesian seaway in a coupled climate model and their relevance to Pliocene climate and El Niño. *Paleoceanography,* **24,** PA1212, doi:10.1029/2008PA001678.

——, S. Yeager, K. Lindsay, K. Moore, and R. Murtugudde, 2010: Quantification of the feedback between phytoplankton and ENSO in the Community Climate System Model. *J. Climate,* **23,** 2916–2925.

Kao, H.-Y., and J.-Y. Yu, 2009: Contrasting eastern Pacific and central Pacific types of ENSO. *J. Climate,* **22,** 615–632.

Lengaigne, M., E. Guilyardi, J.-P. Boulanger, C. Menkes, P. Delecluse, P. Inness, J. Cole, and J. Slingo, 2004: Triggering of El Niño by westerly wind events in a coupled general circulation model. *Climate Dyn.,* **23,** 601–620.

Levitus, S., 1998: *Introduction*. Vol. 1, *World Ocean Database 1998,* NOAA Atlas NESDIS 18, 346 pp.

Liu, Y., X. S. Lian, and R. H. Weisberg, 2007: Rectification of the bias in the wavelet power spectrum. *J. Atmos. Oceanic Technol.,* **24,** 2093–2102.

Liu, Z., and S. Philander, 1995: How different wind stress patterns affect the tropical–subtropical circulations of the upper ocean. *J. Phys. Oceanogr.,* **25,** 449–462.

Luyten, J. R., J. Pedlosky, and H. M. Stommel, 1983: The ventilated thermocline. *J. Phys. Oceanogr.,* **13,** 292–309.

Madden, R. A., and P. R. Julian, 1994: Observations of the 40–50-day tropical oscillation: A review. *Mon. Wea. Rev.,* **122,** 814–837.

McGregor, S., A. Timmermann, N. Schneider, M. F. Stuecker, and M. H. England, 2012: The effect of the South Pacific convergence zone on the termination of El Niño events and the meridional asymmetry of ENSO. *J. Climate,* **25,** 5566–5586.

McPhaden, M. J., 2004: Evolution of the 2002/03 El Niño. *Bull. Amer. Meteor. Soc.,* **85,** 677–695.

——, and Coauthors, 1998: The tropical ocean-global atmosphere observing system: A decade of progress. *J. Geophys. Res.,* **103** (C7), 14 169–14 240.

Meinshausen, M., and Coauthors, 2011: The RCP greenhouse gas concentrations and their extensions from 1765 to 2300. *Climatic Change,* **109,** 213–241, doi:10.1007/s10584-011-0156-z.

Miller, A. J., D. R. Cayan, T. P. Barnett, N. E. Graham, and J. M. Oberhuber, 1994: The 1976–77 climate shift of the Pacific Ocean. *Oceanography,* **7,** 21–26.

Neale, R. B., J. H. Richter, and M. Jochum, 2008: The impact of convection on ENSO: From a delayed oscillator to a series of events. *J. Climate,* **21,** 5904–5924.

Newman, M., S.-I. Shin, and M. Alexander, 2011: Natural variation in ENSO flavors. *Geophys. Res. Lett.,* **38,** L14705, doi:10.1029/2011GL047658.

Pedlosky, J., 1996: *Ocean Circulation Theory*. Springer, 453 pp.

Philip, S., and G. J. van Oldenborgh, 2006: Shifts in ENSO coupling processes under global warming. *Geophys. Res. Lett.,* **33,** L11704, doi:10.1029/2006GL026196.

Rajagopalan, B., and U. Lall, 1998: Interannual variability in western US precipitation. *J. Hydrol.,* **210,** 51–67.

Rasmusson, E., and T. Carpenter, 1982: Variations in tropical sea surface temperature and surface wind fields associated with the Southern Oscillation/El Niño. *Mon. Wea. Rev.,* **110,** 354–384.

Rayner, N. A., P. Brohan, D. E. Parker, C. K. Folland, J. J. Kennedy, M. Vanicek, T. J. Ansell, and S. F. B. Tett, 2006: Improved analyses of changes and uncertainties in sea surface temperature measured in situ since the mid-nineteenth century: The HadSST2 dataset. *J. Climate,* **19,** 446–469.

Ropelewski, C. F., and M. S. Halpert, 1986: North American precipitation and temperature patterns associated with the El Niño/Southern Oscillation. *Mon. Wea. Rev.,* **114,** 2352–2362.

——, and ——, 1996: Quantifying Southern Oscillation–precipitation relationships. *J. Climate,* **9,** 1043–1059.

Smith, T., and R. Reynolds, 2004: Improved extended reconstruction of SST (1854–1997). *J. Climate,* **17,** 2466–2477.

Stevenson, S., 2012: Significant changes to ENSO strength and impacts in the twenty-first century: Results from CMIP5. *Geophys. Res. Lett.,* **39,** L17703, doi:10.1029/2012GL052759.

——, B. Fox-Kemper, M. Jochum, B. Rajagopalan, and S. G. Yeager, 2010: ENSO model validation using wavelet probability analysis. *J. Climate,* **23,** 5540–5547.

——, ——, ——, R. Neale, C. Deser, and G. Meehl, 2012: Will there be a significant change to El Niño in the twenty-first century? *J. Climate,* **25,** 2129–2145.

Sun, D.-Z., 2003: A possible effect of an increase in the warm-pool SST on the magnitude of El Niño warming. *J. Climate,* **16,** 185–205.

——, and T. Zhang, 2006: A regulatory effect of ENSO on the time-mean thermal stratification of the equatorial upper ocean. *Geophys. Res. Lett.,* **33,** L07710, doi:10.1029/2005GL025296.

Taylor, K. E., R. J. Stouffer, and G. A. Meehl, 2012: An overview of CMIP5 and the experiment design. *Bull. Amer. Meteor. Soc.,* **93,** 485–498.

Timmermann, A., J. Oberhuber, A. Bacher, M. Esch, M. Latif, and E. Roeckner, 1999: Increased El Niño frequency in a climate model forced by future greenhouse warming. *Nature,* **398,** 694–697.

——, F.-F. Jin, and M. Collins, 2004: Intensification of the annual cycle in the tropical Pacific due to greenhouse warming. *Geophys. Res. Lett.,* **31,** L12208, doi:10.1029/2004GL019442.

Torrence, C., and G. Compo, 1998: A practical guide to wavelet analysis. *Bull. Amer. Meteor. Soc.,* **79,** 61–78.

Trenberth, K., and J. W. Hurrell, 1994: Decadal atmosphere-ocean variations in the Pacific. *Climate Dyn.,* **9,** 303–319.

Tziperman, E., S. E. Zebiak, and M. A. Cane, 1997: Mechanisms of seasonal–ENSO interaction. *J. Atmos. Sci.,* **54,** 61–71.

Vecchi, G., and B. Soden, 2007: Global warming and the weakening of the tropical circulation. *J. Climate,* **20,** 4316–4340.

Vimont, D. J., J. M. Wallace, and D. S. Battisti, 2003: The seasonal footprinting mechanism in the Pacific: Implications for ENSO. *J. Climate,* **16,** 2668–2675.

Whetton, P., D. Adamson, and M. Williams, 1990: Rainfall and river flow variability in Africa, Australia and east Asia linked to El Niño Southern Oscillation. *Geol. Soc. Aust. Proc. Symp.,* **1,** 71–82.

Wittenberg, A. T., 2009: Are historical records sufficient to constrain ENSO simulations? *Geophys. Res. Lett.,* **36,** L12702, doi:10.1029/2009GL038710.

Xie, S.-P., 1996: Westward propagation of latitudinal asymmetry in a coupled ocean–atmosphere model. *J. Atmos. Sci.,* **53,** 3236–3250.

——, C. Deser, G. Vecchi, J. Ma, H. Teng, and A. Wittenberg, 2010: Global warming pattern formation: Sea surface temperature and rainfall. *J. Climate,* **23,** 966–986.

Yeager, S. G., C. A. Shields, W. G. Large, and J. J. Hack, 2006: The low-resolution CCSM3. *J. Climate,* **19,** 2545–2566.

Yeh, S.-W., J.-S. Kug, B. Dewitte, M.-H. Kwon, B. P. Kirtman, and F.-F. Jin, 2009: El Niño in a changing climate. *Nature,* **461,** 511–514, doi:10.1038/nature08316.

——, B. Kirtman, J.-S. Kug, W. Park, and M. Latif, 2011: Natural variability of the central Pacific El Niño event on multi-centennial timescales. *Geophys. Res. Lett.,* **38,** L02704, doi:10.1029/2010GL045886.

Yu, J.-Y., and H.-Y. Kao, 2007: Decadal changes of ENSO persistence barrier in SST and ocean heat content indices: 1958-2001. *J. Geophys. Res.,* **112,** D13106, doi:10.1029/2006JD007654.

Zebiak, S. E., and M. A. Cane, 1987: A model El Niño-Southern Oscillation. *Mon. Wea. Rev.,* **115,** 2262–2278.